

# Materials Advances

Accepted Manuscript

This article can be cited before page numbers have been issued, to do this please use: A. K. Dhanka, M. Tiwari, P. K. Bhartiya, B. Pani, A. Mittal, D. Mishra and N. Agasti, *Mater. Adv.*, 2026, DOI: 10.1039/D6MA00528D.



This is an Accepted Manuscript, which has been through the Royal Society of Chemistry peer review process and has been accepted for publication.

Accepted Manuscripts are published online shortly after acceptance, before technical editing, formatting and proof reading. Using this free service, authors can make their results available to the community, in citable form, before we publish the edited article. We will replace this Accepted Manuscript with the edited and formatted Advance Article as soon as it is available.

You can find more information about Accepted Manuscripts in the [Information for Authors](#).

Please note that technical editing may introduce minor changes to the text and/or graphics, which may alter content. The journal's standard [Terms & Conditions](#) and the [Ethical guidelines](#) still apply. In no event shall the Royal Society of Chemistry be held responsible for any errors or omissions in this Accepted Manuscript or any consequences arising from the use of any information it contains.

## Modulation of oxygen vacancies influences electrocatalytic performance of Ni-doped Ceria for oxygen and hydrogen evolution

Ajit Kumar Dhanka<sup>a</sup>, Mayank Tiwari<sup>b</sup>, Prashant K. Bhartiya<sup>c</sup>, Balaram Pani<sup>d</sup>, Avneesh Mittal<sup>e</sup>, Debabrata Mishra<sup>\*b</sup>, and Nityananda Agasti<sup>\*a</sup>

<sup>a</sup> Department of Chemistry, University of Delhi, North Campus, Delhi 110007, India

<sup>b</sup> Department of Physics and Astrophysics, University of Delhi, North Campus, Delhi 110007, India

<sup>c</sup> Delhi School of Climate Change and Sustainability, Institution of Eminence, University of Delhi, 110007

<sup>d</sup> Department of Chemistry, Bhashkaracharya College of Applied Sciences, University of Delhi, Dwarka, New Delhi, 110075, India.

<sup>e</sup> Department of Electronic Sciences, Bhashkaracharya College of Applied Sciences, University of Delhi, Dwarka, New Delhi, 110075, India.

### Abstract

The development of high-performance catalysts for electrochemical water splitting continues to drive advancements in sustainable hydrogen production. Ceria-based materials being potential catalysts owing to their remarkable redox behaviour, modulation of defects in ceria is an effective strategy for efficient electrocatalytic water splitting. Thus, aiming to study the creation of oxygen vacancies as a function of dopant concentration, this report demonstrates enhanced electrocatalytic water splitting by regulating defects in ceria via Nickel doping. Nickel-doped ceria creates a bifunctional electrocatalyst with enhanced activity for both oxygen and hydrogen evolution. This improvement stems from interfacial interactions between Ni and the CeO<sub>2</sub>, which enhances oxygen vacancy defects in ceria. Mechanistic insights derived by a range of spectroscopic techniques reveal enhancement in oxygen vacancies in ceria with the increase in the concentration of dopant. Photoluminescence (PL) studies reveal suppressed charge recombination, indicating



efficient electron-hole separation facilitated by the defects. The defect regulated electrocatalytic performance has been established via electrocatalytic hydrogen evolution reaction (HER) and oxygen evolution reaction (OER) with the evolution of H<sub>2</sub> and O<sub>2</sub> quantitatively estimated, using Ni doped CeO<sub>2</sub> and undoped CeO<sub>2</sub>. Notably, doping of Ni brings in significant reduction in overpotentials by 87 mV for oxygen evolution and 59 mV for hydrogen evolution. Alongside, current densities also experience substantial increase by 166 mA/cm<sup>2</sup> for oxygen evolution and 96 mA/cm<sup>2</sup> for hydrogen evolution. The reduction in Tafel slope from 381 to 199 mV/dec for OER and from 334 to 217 mV/dec for HER, indicates faster reaction kinetics. Chronoamperometric measurement reveals notable electrochemical stability of the electrocatalyst Ni doped CeO<sub>2</sub>. This study on defect-structure related electrocatalysis provides insight into the dopant regulated defect generation in ceria-based materials for designing electrocatalysts for effective water splitting.

**Keywords:** Ni-doped CeO<sub>2</sub>, Ni/CeO<sub>2</sub>, Ceria, Oxygen vacancies, electrocatalysis, water splitting, hydrogen evolution reaction (HER), and oxygen evolution reaction (OER).

## 1.0 Introduction

Fossil fuels such as coal, natural gas, and petroleum have long been crucial in fulfilling global energy requirements, supporting industries, transportation, and daily life. However, the growing global population and rapid industrialization have led to an overreliance on these non-renewable resources, raising concerns about future shortages<sup>1,2</sup>. Experts predict that crude oil reserves may be exhausted within 40 to 50 years<sup>3</sup>, coal production is expected to peak between 2042 and 2062<sup>4</sup>, and the demand for clean energy is projected to increase by 50% by 2030<sup>5</sup>. Given these challenges, hydrogen has emerged as a promising alternative energy source due to its high energy yield and zero carbon emissions<sup>6,7,8</sup>. One of the most economical methods for producing hydrogen is steam reforming; however, it faces significant environmental challenges. These include the formation of significant amounts of carbonaceous byproducts, expansive methods, severe reaction conditions, and the dependence on an external heat transfer system to maintain the reaction<sup>9, 10,11</sup>. Additionally, producing 1 kilogram of hydrogen releases nearly 9 kilograms of carbon dioxide<sup>12</sup>. A more sustainable approach is electrochemical water splitting<sup>13</sup>, which involves two key reactions: the hydrogen evolution reaction (HER) to generate hydrogen and the oxygen evolution reaction (OER) to produce oxygen<sup>14,15,16</sup>. Despite its potential, the efficiency of this method is hindered by high



overpotentials, sluggish reaction kinetics, and the need for cost-effective and durable catalysts. Recent research has focused on semiconductor metal oxides as promising electrocatalysts for water splitting<sup>17,18,19,,20,21,22,23</sup>. Among these, cerium oxide ( $\text{CeO}_2$ ) has gained significant attention due to its exceptional redox properties, attributed to the coexistence of  $\text{Ce}^{3+}$  and  $\text{Ce}^{4+}$  oxidation states. This redox behavior facilitates the creation of oxygen vacancies in the  $\text{CeO}_2$  lattice, represented as  $\text{Ce}^{4+}\text{-O}_v\text{-Ce}^{3+}$  (where  $\text{O}_v$  denotes an oxygen vacancy). These vacancies enhance the catalytic performance of  $\text{CeO}_2$  in various electrochemical applications<sup>24,25</sup>. Additionally,  $\text{CeO}_2$ , being an n-type semiconductor with a band gap of around 3.2-3.3 eV<sup>26</sup>. However, its wide band gap presents a limitation; the density of reactive charge carriers is insufficient for electrocatalytic reaction<sup>27</sup>. This necessitates the development of band gap-engineered ceria nanostructures with tailored electronic properties to enhance their suitability for electrocatalytic applications<sup>28,29,30</sup>. Recent advancements in ceria-based nanomaterials have focused on tuning the band gap and increasing surface defects to enhance light absorption and to minimize recombination of photogenerated electron ( $e^-$ ) and hole ( $h^+$ ) pairs. Ghosh et al. have demonstrated that incorporating defects into ceria heterojunction catalysts significantly improves their performance in hydrogen evolution. The improvement arises from their ability to capture a wider portion of the visible spectrum, facilitate more effective separation and migration of charge carriers, and adjust the electronic structure to favor the reaction process<sup>31</sup>. Our research group has recently demonstrated that incorporating silver into the ceria lattice effectively generates oxygen vacancies via defects, which in turn leads to a marked improvement in overall water-splitting performance<sup>32</sup>. Furthermore,  $\text{CeO}_2$  serves as an effective catalyst support, enabling the integration of metal or metal oxide nanoparticles (NPs) to form heterojunctions. The introduction of metal nanoparticles onto ceria ( $\text{CeO}_2$ ) surfaces forms well-defined metal-ceria interfaces, which are known to enhance interfacial charge transfer and thereby improve electrocatalytic performance in water-splitting reactions. These interfaces enhance electrical conductivity and catalytic activity by modifying the electronic structure of ceria and stabilising reactive intermediates. Among commonly used transition metals such as Ag, Au, Cu, Fe, and Ni, Ni stands apart due to its strong metal-support interaction with ceria<sup>33,34,35,36,37,38</sup>. Doping Ni into ceria significantly increases the density of surface oxygen vacancies. These vacancies serve as critical active sites that enhance the water-splitting kinetics. Furthermore, the doped Ni modifies the electronic band structure of ceria by reducing its band gap, thus facilitating improved electrical conductivity and charge transport under electrochemical operating



conditions<sup>39,40</sup>. Notably, Ni is a ferromagnetic material, and its magnetic properties also contribute to the formation of triplet-state molecular oxygen ( $^3\text{O}_2$ ) during the OER. Ni could provide a pool of spin-polarized electrons which promotes the formation of  $^3\text{O}_2$  by lowering the energy barrier required for the formation of triplet oxygen<sup>41,42,43</sup>. Thus, Ni doping in ceria can introduce a combination of, (i) structural defects (oxygen vacancies), (ii) electronic modifications (band gap narrowing), and (iii) spin-related phenomena (triplet  $\text{O}_2$  generation), all of which can synergistically improve the electrocatalytic activity of ceria for water splitting reactions.

Though ceria-based catalysts have been studied for energy applications, comprehensive investigations into the nature of defects within ceria and their influence on electrocatalytic performance, especially in OER and HER, remain scarce. Most existing literature offers limited insight into the detailed structural analysis of these defects and their direct mechanistic contributions to catalytic performance<sup>44,45,46,47</sup>. Therefore, this study aims to address these gaps by providing an in-depth examination of the structural defects in ceria-based materials and exploring their specific roles in enhancing the water splitting kinetics. Further, there has been a very limited study on the effect of concentration of oxygen vacancies on electrocatalytic activities of the ceria-based materials. To address this gap, herein we attempt to investigate the defect dependent electrocatalytic performance of ceria-based materials. We have synthesized the Ni-doped  $\text{CeO}_2$  via a solvothermal method with varying nickel concentrations (1%, 5%, and 10%), to study their electrocatalytic performance for water splitting. Compared to pristine  $\text{CeO}_2$ , the Ni-doped  $\text{CeO}_2$  samples exhibit progressively improved electrocatalytic activity with increasing concentration of Ni, owing to; (i) enhanced defect formation, (ii) improved charge transfer, and (iii) a greater density of active surface sites. Among all samples, the 10% Ni/ $\text{CeO}_2$  catalyst exhibits the most optimized electrocatalytic performance, achieving a notable reduction in overpotential of 87 mV for OER and 59 mV for the HER compared to pristine  $\text{CeO}_2$ . Additionally, it shows substantial improvements in current density, with a 66% enhancement for OER and a 140% enhancement for HER. This enhancement highlights the crucial role of Ni concentration in tuning the electrocatalytic efficiency of ceria-based systems. Furthermore, characterization studies reveal that Ni incorporation induces defect states and lattice expansion due to charge imbalance, stemming from the variable oxidation states of Ni. These defects increase surface oxygen vacancies, which act as electron traps, suppressing recombination and promoting charge carrier separation. Additionally, the band gap decreases progressively with Ni content: from 3.31 eV for  $\text{CeO}_2$  to



3.23, 3.11, and 3.03 eV for 1%, 5%, and 10% Ni-doped CeO<sub>2</sub>, respectively. The synergistic interaction between Ni and CeO<sub>2</sub> enhances the structural and electronic properties of Ni-doped CeO<sub>2</sub>, thereby improving its overall electrocatalytic activity. A plausible reaction pathway is proposed to elucidate the mechanistic role of Ni-doped CeO<sub>2</sub> in facilitating both hydrogen and oxygen evolution, emphasizing the significance of doped metal and ceria interactions in advancing next-generation catalysts for sustainable hydrogen production.

## 2.0 EXPERIMENTAL SECTION

### 2.1 Materials

During this research, all reagents used were commercially available and utilized without any further purification. Cerium nitrate hexahydrate (Ce(NO<sub>3</sub>)<sub>3</sub>·6H<sub>2</sub>O, 99%), sodium hydroxide (NaOH, 98%), ethanol (C<sub>2</sub>H<sub>5</sub>OH), methanol (CH<sub>3</sub>OH), Nickel foam (NF), potassium hydroxide (KOH), polyvinylidene fluoride (PVDF), carbon black, and methanol (CH<sub>3</sub>OH) were procured from Sigma-Aldrich India, while nickel nitrate hexahydrate (Ni(NO<sub>3</sub>)<sub>2</sub>·6H<sub>2</sub>O) was obtained from Merck India.

### 2.2 Preparation of Ni-doped CeO<sub>2</sub>

The Ni-doped CeO<sub>2</sub> were synthesized by a solvothermal method<sup>48</sup>, using cerium nitrate (Ce(NO<sub>3</sub>)<sub>3</sub>·6H<sub>2</sub>O) and nickel nitrate (Ni(NO<sub>3</sub>)<sub>2</sub>·6H<sub>2</sub>O) as precursors. In a typical preparation method cerium nitrate and nickel nitrate were dissolved in 50 mL of methanol. The mixed solution was kept on constant magnetic stirring to make it homogeneous. 0.25 g of sodium hydroxide dissolved in 10 ml of methanol in a separate beaker, was added dropwise into the mixed solution with continuous stirring for 30 minutes. After being stirred, the mixed solution was transferred into a Teflon-lined stainless-steel autoclave and heated for 18 hours at 180 °C in an oven. The autoclave on naturally cooling to room temperature, the obtained colloidal solution was centrifuged at 8000 rpm for 5 minutes and washed with ethanol 3-4 times. Finally, the precipitate obtained was dried at 80 °C overnight and subsequently put for calcination at 250 °C for 2 hours to obtain Ni-doped CeO<sub>2</sub> (Ni/CeO<sub>2</sub>). To study the effect of Ni concentration on the defects in CeO<sub>2</sub>, Ni doped CeO<sub>2</sub> was prepared with varied concentration of Ni; 1% (6.6 mg), 5% (33.4 mg), 10% (66.8 mg) (Ni (NO<sub>3</sub>)<sub>2</sub>·6H<sub>2</sub>O) was mixed into (1.0 g) Ce (NO<sub>3</sub>)<sub>3</sub>·6H<sub>2</sub>O. For comparison, CeO<sub>2</sub> nanoparticles were prepared by the same procedure, except the addition of nickel nitrate.



### 2.3. Fabrication of electrodes for electrochemical measurements

The electrodes were fabricated using the drop-casting method, where CeO<sub>2</sub> and Ni/CeO<sub>2</sub> were applied onto Nickel foam (NF). The first electrode was prepared by drop-casting CeO<sub>2</sub> as the active material, polyvinylidene fluoride (PVDF) as the binder, and carbon black as the conducting agent in a ratio of 85:10:5, respectively. Similarly, additional electrodes were prepared using Ni/CeO<sub>2</sub>, maintaining the same composition ratio. To study the effect of varied concentrations of dopant (Ni) on the electrocatalytic performance, electrodes were prepared with Ni/CeO<sub>2</sub> with Ni concentrations 1%, 5%, and 10%. The Ni/CeO<sub>2</sub> materials were coated onto Nickel foam, covering an area of 1 cm<sup>2</sup> using the drop-casting technique. After coating, the electrodes were placed in a vacuum oven at 80° C for 10 hours to ensure proper drying, followed by natural cooling to room temperature. The fabricated electrodes were designated as NF (bare Nickel Foam), NF/CeO<sub>2</sub> (CeO<sub>2</sub>-coated on Nickel Foam), NF/1% Ni/CeO<sub>2</sub> (1% Ni doped CeO<sub>2</sub> coated on Nickel Foam), NF/5% Ni/CeO<sub>2</sub> (5% Ni doped CeO<sub>2</sub> coated on Nickel Foam), and NF/10% Ni/CeO<sub>2</sub> (10% Ni doped CeO<sub>2</sub> coated on Nickel Foam).

### 2.4 Sample Characterizations

To study the structural and morphological features of the synthesized materials, multiple characterization techniques were considered. Ni/CeO<sub>2</sub> and CeO<sub>2</sub> were characterized by Powder X-ray diffraction (PXRD) to understand the crystalline pattern of the composites using FEI Quanta 200 F SEM diffractometer with Cu K radiation, ( $\lambda = 0.1542$  nm) in the  $2\theta$  range of 20-90. Vibrational spectra of the samples were collected by using Nicolet™ iS50 Fourier-Transform Infrared (FTIR) Spectrometer in the wavelength range 500–4000 cm<sup>-1</sup> with KBr pellets. To understand the optical behavior of the materials, UV-visible absorbance spectra were recorded by Spectrophotometer Shimadzu 1800, and UV–vis diffuse reflectance spectra (DRS) using Agilent Cary 5000. Raman spectroscopy (Laser Raman Spectrometer Model Invia II) was carried out to study defects in the materials. The morphological character of the Ni/CeO<sub>2</sub> and CeO<sub>2</sub> were examined using Field Emission Scanning Electron Microscopy (FESEM) with Oxford-EDX system IE 250 X Max 80 (FEI Quanta 200 F SEM). The elemental composition of the samples was analyzed by Energy Dispersive X-ray spectroscopy (EDX). Moreover, to gain a thorough



insight into packing pattern of Ni/CeO<sub>2</sub>, high resolution transmission electron microscopy (HRTEM) images were collected using Transmission Electron Microscope *TECNAI G20 HR-TEM* 200kV. Thermogravimetric analysis (TGA) was performed on HiRes1000 RT to 1100C with heating rate of 10 °/min to determine thermal stability of the materials. Surface area, pore size and pore volume were analyzed by the Autosorb-iQ XR system (Quantachrome Instruments). Before measurement, the samples underwent degassing at 150 °C for 10 hours under high vacuum conditions ( $\sim 1 \times 10^{-5}$  bar) to eliminate any physisorbed contaminants. The adsorption–desorption isotherms were then acquired at 77 K using liquid nitrogen to maintain a stable cryogenic environment for precise analysis. The surface elemental oxidation state and composition was analyzed by X-ray photoelectron spectroscopy (XPS) using a Kratos Axis Supra Plus XPS equipped with a monochromatic Al K $\alpha$  X-ray source (1486.6 eV). The high-resolution data was charge corrected to the reference C 1s signal at 284.5 eV. The photoluminescence (PL) analysis was performed at ambient condition using a Horiba Yvon PTI QuantaMaster (8450-11) spectrophotometer, where a nano-LED was utilized as the excitation light source. The electron spin resonance (ESR) spectra of the powdered samples were obtained using a JEOL JES-X320 X-band spectrometer operating at room temperature. The measurements were performed under the following conditions: a microwave frequency of 9.17 GHz, modulation frequency of 100 kHz, scan range of 1300 mT, and a center field of 3270.00 G. Electrochemical measurements, including Linear Sweep Voltammetry (LSV), electrochemical impedance spectroscopy (EIS), and Chronoamperometry, were performed in an alkaline medium using a CS350 Corr-Test electrochemical workstation (Potentiostat) under a standard three-electrode configuration. A Platinum (Pt) electrode served as the counter electrode, while an Ag/AgCl electrode was the reference electrode. To ensure consistency in potential values, they were converted to the reversible hydrogen electrode ( $E_{\text{RHE}}$ ) using the Nernst equation<sup>49</sup>. All electrochemical measurements were performed in a 1 M KOH solution, which served as the electrolyte. The quantification of hydrogen (H<sub>2</sub>) and oxygen (O<sub>2</sub>) gases was conducted in a tightly sealed Hoffmann apparatus.

### 3 Results and discussion.

#### 3.1 Structure, morphology and elemental analysis.

The prepared Ni-doped CeO<sub>2</sub> (Ni/CeO<sub>2</sub>) and CeO<sub>2</sub> were analyzed using UV-vis absorption spectra (Fig. 1a). The band observed at a wavelength of 301 nm is characteristic of CeO<sub>2</sub> nanoparticles<sup>50</sup>.



However, in the spectrum of the doped CeO<sub>2</sub>, with increased concentration of Ni dopant, the band shifts towards the visible region. It exhibits a red shift in the absorption band from 301 nm to 323 nm due to the absorption edge induced by the incorporation of Ni<sup>51</sup> (Fig. S1 ESI). The peak shifting in doped CeO<sub>2</sub> indicates a decrease in the band gap and crystallite size<sup>52,53,54</sup>. Furthermore, the interaction of Ni with the ceria lattice induces the formation of oxygen vacancies and enhances the reduction of Ce<sup>4+</sup> to Ce<sup>3+</sup>. The increased presence of Ce<sup>3+</sup> species gives rise to localised electronic states that emerge near the conduction band, which ultimately leads to a reduction in the energy band gap in doped ceria<sup>55</sup>. The direct energy band gap (E<sub>g</sub>) of Ni/CeO<sub>2</sub> and CeO<sub>2</sub> was calculated using UV-vis diffuse reflectance spectroscopy (DRS) using the Kubelka-Munk (K-M) function. To minimize the effects of light scattering in the DRS spectra and ensure accurate band gap measurements for solid materials, the Kubelka-Munk (K-M) function was utilized. The band gap plot obtained from the K-M function relates to the energy of the photons. The E<sub>g</sub> values for CeO<sub>2</sub> and Ni-doped CeO<sub>2</sub> were specifically determined from the point where a linear fit of the Kubelka-Munk function intersects the abscissa axis, using Eq.  $\alpha h\nu = A (h\nu - E_g)^{n/2}$ .

Where  $\alpha$  is the absorption coefficient, A is a constant, h is Planck's constant,  $\nu$  denotes the frequency of light, and E<sub>g</sub> corresponds to the band gap energy<sup>56</sup>. The DRS spectra reveals that the estimated band gap energies (E<sub>g</sub>) 3.03, 3.11, 3.23 and 3.31 eV for 10%, 5%, 1% Ni/CeO<sub>2</sub> and CeO<sub>2</sub>, respectively (Fig. 1b). The observed reduction in band gap in Ni doped CeO<sub>2</sub> can be attributed to the incorporation of Ni in the CeO<sub>2</sub> lattice facilitating electron excitation from the conduction band to the valence band, which is consistent with findings in the literature<sup>57,58</sup>. Also, the incorporation of Ni ions leads to the creation of interstitial sites, because Ni<sup>2+</sup>/Ni<sup>3+</sup> ions replace Ce<sup>4+</sup> in the CeO<sub>2</sub> lattice. These interstitial sites introduce defect or impurity energy levels between the valence and conduction bands of CeO<sub>2</sub>, facilitating the electron transition<sup>59</sup>.

To confirm the formation of Ni-doped CeO<sub>2</sub> from structural characteristics, powder X-ray diffraction (PXRD) analysis was conducted in the 2 $\theta$  range 20 to 80°. The eight peaks observed at 2 $\theta$  angles, 28.4, 32.9, 47.5, 56.3, 59.0, 69.3, 76.7, and 78.8 correspond to the (111), (200), (220), (311), (222), (400), (331), and (420) planes of CeO<sub>2</sub> crystals (Fig. 1c). The sharpness of these XRD peaks in the synthesized nanoparticles indicates the formation of a crystalline phase with no impurities or secondary phases detected within the instrumental limits and these peaks match with the cubic fluorite structure of CeO<sub>2</sub> (JCPDS card data 34-0394)<sup>60</sup>. No additional diffraction peak Ni was observed after the addition of Ni into CeO<sub>2</sub>. However, there is a decrease in the peak



intensity and broadening of the peaks, on increasing the concentration of dopant (1, 5 and 10%) Ni in CeO<sub>2</sub> (Fig. S2a ESI). This indicates the formation of crystal defects around the dopant atoms. Also, the substitution of Ni ions appears to have inhibited the growth of CeO<sub>2</sub> nanoparticles and thus degraded their crystal quality<sup>61</sup>. Moreover, there is a reduction in crystallite size, which is evident from the change in full-width at half-maximum (FWHM)<sup>62</sup>. Compared to pristine CeO<sub>2</sub>, the FWHM of the (111) peak is higher in Ni-doped ceria. Further, in Ni-doped CeO<sub>2</sub>, the FWHM of the (111) peak increases with an increase in the concentration of Ni. This suggests that the incorporation of Ni into the CeO<sub>2</sub> lattice can be attributed to the creation of defects in doped ceria<sup>63</sup>. Besides an increase in the FWHM, there is a slight downshift of the (111) peak in Ni-doped CeO<sub>2</sub> compared to pristine CeO<sub>2</sub> (Table-1). The crystallite size of pristine ceria and doped ceria was estimated by the Scherrer equation<sup>64</sup>,  $D = K\lambda / \beta \cos\theta$ , where D represents the crystallite size, K is a dimensionless shape factor, often taken as 0.98 for spherical crystals,  $\lambda$  denotes the wavelength of the X-ray (typically 1.54 Å for copper K $\alpha$  radiation),  $\beta$  is the full-width at half-maximum (FWHM) of the peak (111) and  $\theta$  is the Bragg angle (half of the 2 $\theta$  angle where the peak occurs). The crystallite size of ceria was calculated to be 8.35 nm for pristine CeO<sub>2</sub> nanoparticles and 3.77, 3.67 and 3.66 nm for 1, 5 and 10% of Ni-doped CeO<sub>2</sub>, respectively. Additionally, incorporation of Ni of concentration up to 10%, into CeO<sub>2</sub>, the X-ray diffraction (XRD) patterns typically show no extra peaks, indicating that Ni ions are successfully integrated into the CeO<sub>2</sub> matrix without forming separate phases. This suggests substitutional doping of Ni into the CeO<sub>2</sub> lattice and the formation of a single-phase material. However, when the concentration of Ni exceeds 10%, diffraction peaks corresponding to the NiO begin to appear<sup>65</sup>, indicating the formation of a secondary phase (NiO) in addition to the CeO<sub>2</sub> structure,<sup>66</sup> which is shown in Fig. S2b and c ESI.

**Table 1:** Detailed values of (111) peak position, FWHM, and crystallite size of CeO<sub>2</sub> and Ni doped CeO<sub>2</sub>.

Materials	Peak position (2 $\theta$ )	FWHM	Crystallite size (nm)
10% Ni/CeO <sub>2</sub>	28.70	2.34	3.66
5% Ni/CeO <sub>2</sub>	28.71	2.33	3.68
1% Ni/CeO <sub>2</sub>	28.69	2.27	3.77



CeO <sub>2</sub>	28.74	1.02	8.35
------------------	-------	------	------

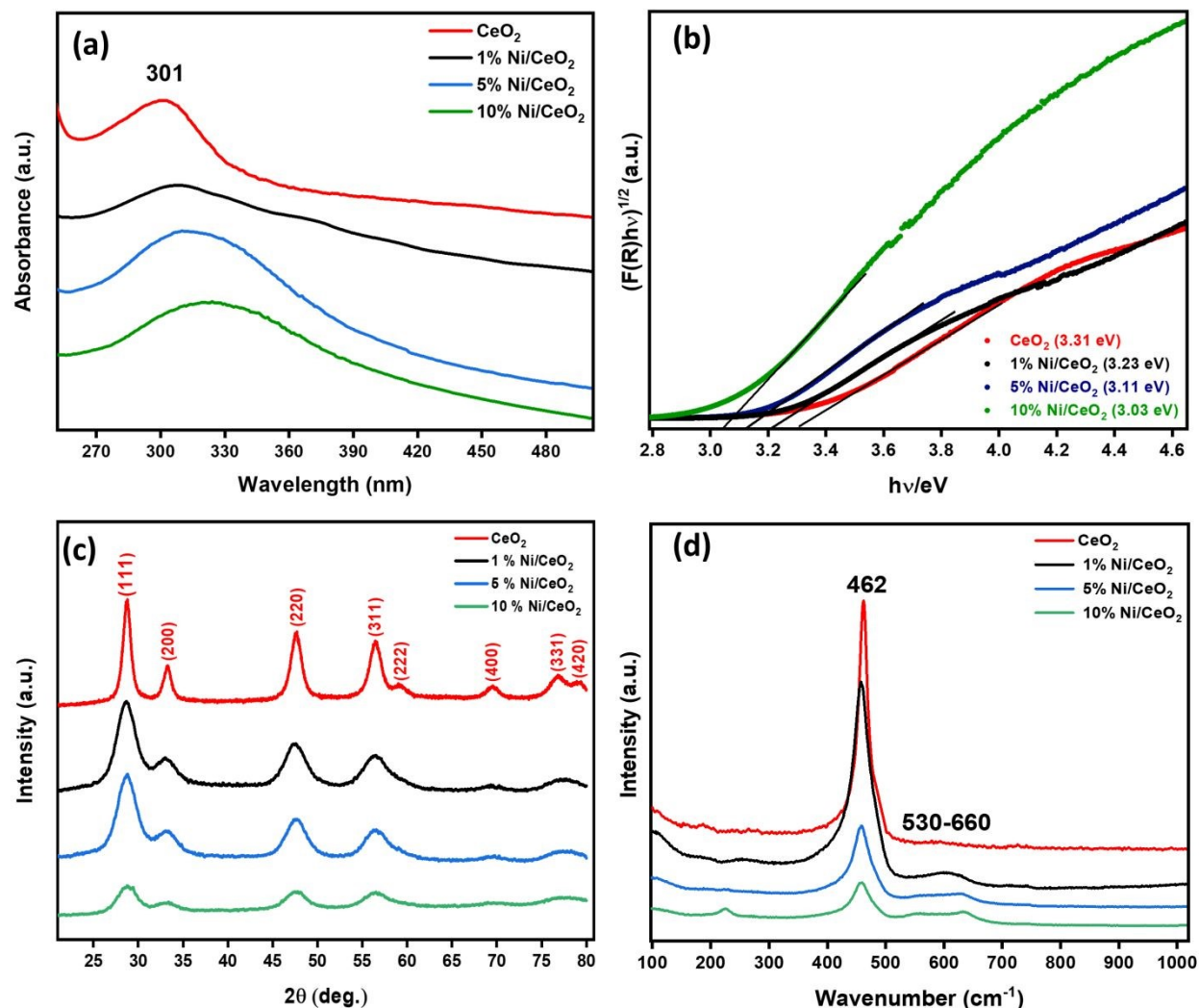


**Fig. 1** (a) UV–vis absorption spectra, (b) Calculated band gap energy using UV–Vis DRS by Kubelka-Munk (K-M) function, (c) PXRD spectra and (d) Raman spectra for CeO<sub>2</sub> and 1,5,10% Ni/CeO<sub>2</sub>.

The Raman spectroscopy is a non-destructive technique to characterize nanomaterials and the defects in them. So, to ascertain the oxygen vacancy formed in CeO<sub>2</sub> due to Ni doping, Raman spectra of CeO<sub>2</sub> and Ni-doped CeO<sub>2</sub> were measured in the range of 100-1020 cm<sup>-1</sup> shown in Fig. 1d. Pristine CeO<sub>2</sub> typically exhibits a prominent Raman peak at 462 cm<sup>-1</sup>, corresponding to the Raman-active vibrational mode (F<sub>2g</sub>), a characteristic of the fluorite structure<sup>67</sup>. 1, 5, and 10% Ni



doped CeO<sub>2</sub> displayed a strong Raman peak in this region, confirming the preservation of the fluorite structure of ceria. Additionally, the appearance of the bands in the region, 530-660 cm<sup>-1</sup> corresponds to a defect-induced mode (D)<sup>68</sup>, which is associated with the oxygen vacancies<sup>56</sup> (Fig. S3b ESI). The D bands (highlighted with a pink region), which are not so prominent in the pristine CeO<sub>2</sub>, indicate an increase in oxygen vacancies with an increase in the concentration of the dopant Ni. Moreover, the intensity of the characteristic F<sub>2g</sub> peak for Ce-O at 462 cm<sup>-1</sup> decreases with increase in the concentration of dopant, Ni in CeO<sub>2</sub>. Besides, the F<sub>2g</sub> peak also suffers downshift towards lower wavenumber from 462 cm<sup>-1</sup> (CeO<sub>2</sub>) to 458 cm<sup>-1</sup> for 10% Ni-doped CeO<sub>2</sub> (Fig. S3a ESI). The decrease in intensity and downshift of the F<sub>2g</sub> peak suggest an increase in oxygen vacancies in Ni/CeO<sub>2</sub>. The increase in oxygen vacancy in CeO<sub>2</sub> is represented by an increase in Ce<sup>3+</sup> concentration. Compared to pristine CeO<sub>2</sub>, there is an increase in Ce<sup>3+</sup> in Ni-doped CeO<sub>2</sub>, which is also confirmed from the expansion of the crystal lattice. The incorporation of dopant Ni has led to an increase in the concentration of Ce<sup>3+</sup> ions in ceria, resulting in a notable expansion of the crystal lattice. This expansion is attributed to the larger ionic radius of Ce<sup>3+</sup> compared to Ce<sup>4+</sup><sup>69</sup>. The lattice expansion is further evidenced by the observed decrease in the Full Width at Half Maximum (FWHM) of the F<sub>2g</sub> peaks in doped CeO<sub>2</sub>. This reduction in FWHM indicates an increase in crystallite size, which is consistent with the lattice expansion caused by the higher proportion of Ce<sup>3+</sup> ions. The presence of more Ce<sup>3+</sup> ions not only affects the lattice parameters but also influences the overall crystal structure and properties of the doped ceria materials. These structural changes have significant implications for the materials' oxygen storage capacity and crystallite size. The crystallite sizes of CeO<sub>2</sub> and doped CeO<sub>2</sub> were calculated by the equation<sup>70,71</sup>  $\Gamma$  (cm<sup>-1</sup>) = 5 + 51.8/ d(nm), where  $\Gamma$  represents the Half width at Half Maximum (HWHM), and d is the crystallite size in nanometers for CeO<sub>2</sub> and Ni-doped CeO<sub>2</sub> samples. The crystallite size was determined to be 12.04 nm for pristine CeO<sub>2</sub>, and 4.84 nm, 4.71 nm, and 4.50 nm for 1%, 5%, and 10% Ni-doped ceria, respectively. The difference in the crystallite sizes obtained from X-ray Diffraction (XRD) and Raman studies can be ascribed to the fundamental differences in the underlying principles of these techniques. The Scherrer analysis, based on X-ray diffraction (XRD), provides an estimate of the coherent diffraction domain size, which may be affected by factors such as lattice strain, instrumental broadening, and defects within the crystal structure. In contrast, Raman spectroscopy determines crystallite size through phonon confinement effects, which are more sensitive to local structural ordering and short-range interactions.



Furthermore, the broad band observed at 530-660  $\text{cm}^{-1}$  in the Raman spectra confirms the highly disordered nature of doped  $\text{CeO}_2$ . To analyze the broad band range at 530-660  $\text{cm}^{-1}$ , it was deconvoluted using a Gauss fitting, resulting the calculated area under the band (Fig. 2). The under area of bands increased (Table 2), on increasing the concentration of Ni into  $\text{CeO}_2$  which corresponds to the oxygen vacancies (Fig. 2). Moreover, increase in the oxygen vacancies and lattice disorder, ultimately leads to an increase in surface defects. Additionally, the observed ratio of the integrated area of the D band to that of the  $\text{F}_{2\text{g}}$  peak ( $I_{\text{D}}/I_{\text{F}_{2\text{g}}}$ ) serves as an indicator of the relative concentration of oxygen vacancies on the surface of doped  $\text{CeO}_2$  and pristine  $\text{CeO}_2$ . A notable increase in the ( $I_{\text{D}}/I_{\text{F}_{2\text{g}}}$ ) ratio is observed for the doped  $\text{CeO}_2$ , suggesting a higher density of oxygen vacancies compared to pristine  $\text{CeO}_2$ . The calculated  $I_{\text{D}}/I_{\text{F}_{2\text{g}}}$  ratio is 0.006, 0.033, 0.116, and 0.316 for  $\text{CeO}_2$  and 1%, 5%, 10% Ni/ $\text{CeO}_2$ , respectively, as illustrated in Table 2 and Fig. 2. This enhanced  $I_{\text{D}}/I_{\text{F}_{2\text{g}}}$  ratio can be attributed to the strong interfacial interactions between Ni and  $\text{CeO}_2$ , which promote defect formation in doped ceria.



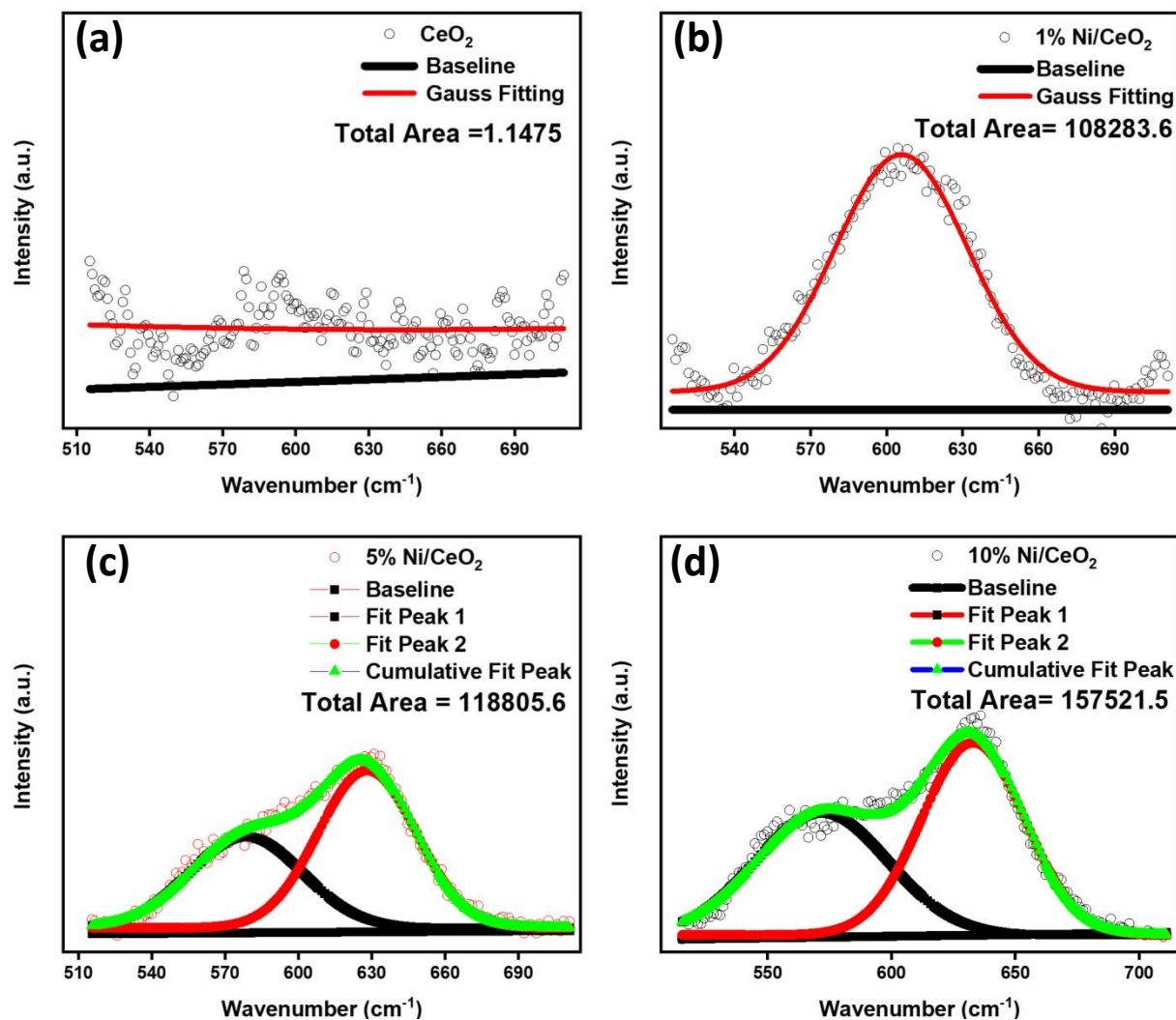


Fig.2 Deconvolution of Raman Spectra for (a)  $\text{CeO}_2$  and (b), (c), & (d) for 1%, 5%, 10% Ni/ $\text{CeO}_2$ , respectively.

**Table 2:** Detailed values of  $F_{2g}$  peak position, HWMH, crystallite size, total area of D band, and calculated ratio of  $I_D/I_{F_{2g}}$  in Raman spectra for  $\text{CeO}_2$  and Ni-doped  $\text{CeO}_2$ .

Materials	Peak position ( $\text{cm}^{-1}$ )	HWHM	Crystallite size (d)	Total area of the D band	$I_D/I_{F_{2g}}$
10% Ni/ $\text{CeO}_2$	458	16.5	4.50 nm	157521.5	0.316
5% Ni/ $\text{CeO}_2$	459	16.0	4.71 nm	118805.6	0.116
1% Ni/ $\text{CeO}_2$	459.3	15.7	4.84 nm	108283.6	0.033
$\text{CeO}_2$	462	9.3	12.04 nm	1.14	0.006



Further, to ascertain the formation of oxygen vacancies in Ni-doped CeO<sub>2</sub> (Ni/CeO<sub>2</sub>), the photoluminescence (PL) spectra of CeO<sub>2</sub> and Ni-doped CeO<sub>2</sub> (Ni/CeO<sub>2</sub>) were measured in the wavelength range of 200–800 nm using an excitation wavelength of 532 nm, as shown in Fig. 3a. The PL emission intensities of pristine CeO<sub>2</sub> and Ni/CeO<sub>2</sub> display distinct trends, reiterating the doping of Ni in CeO<sub>2</sub>. Compared to Ni/CeO<sub>2</sub>, pristine CeO<sub>2</sub> exhibits higher PL intensity at wavelength 532 nm, corresponding to its larger bandgap energy ( $E_g = 3.31$  eV). Further, the PL intensity decreases with Ni doping in CeO<sub>2</sub>. As the Ni concentration increases, the PL peak intensity decreases progressively, following the trend: CeO<sub>2</sub> > 1% Ni/CeO<sub>2</sub> > 5% Ni/CeO<sub>2</sub> > 10% Ni/CeO<sub>2</sub>. This decline in PL intensity with increasing Ni doping can be attributed to the increase in defects, such as oxygen vacancies (Ce<sup>+3</sup>), on the surface of CeO<sub>2</sub><sup>72,73</sup>. Notably, the 10% Ni/CeO<sub>2</sub> sample exhibits the lowest emission intensity, indicating a higher concentration of oxygen vacancies, which suggests that electron-hole recombination is effectively suppressed<sup>74</sup>. The suppression in the recombination of electron-hole is due to their efficient separation, which can be attributed to the interaction between Ni and CeO<sub>2</sub>, resulting in the superior electrocatalytic efficiency of 10% Ni/CeO<sub>2</sub><sup>75</sup>.

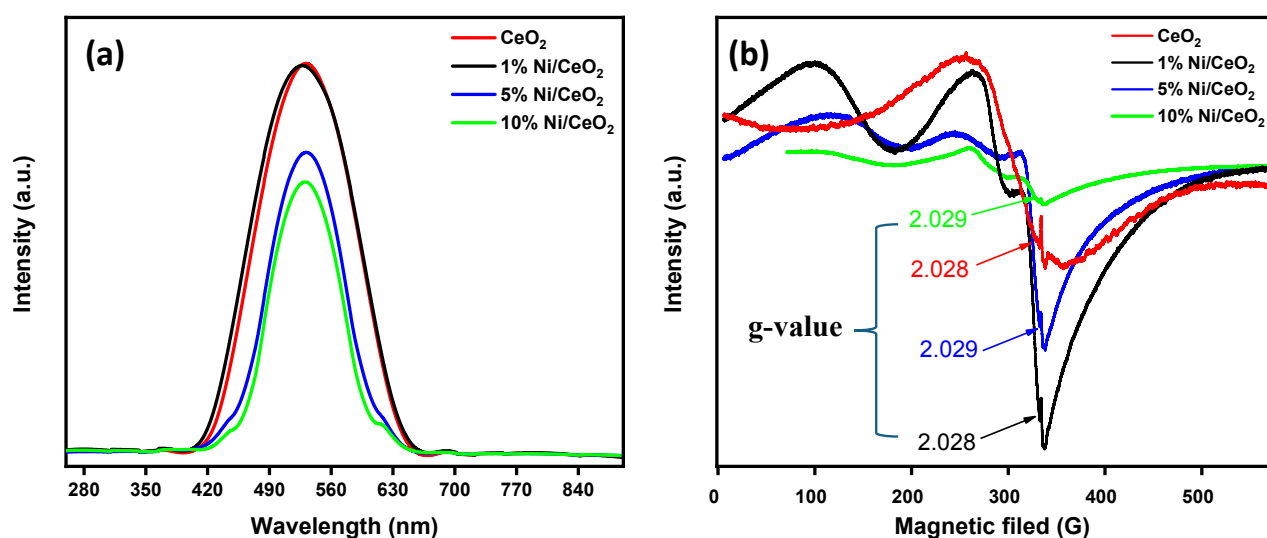


Fig. 3. PL (a) and EPR (b) spectra (inset calculated g-values) of CeO<sub>2</sub> and 1,5,10% Ni/CeO<sub>2</sub>.



Electron Paramagnetic Resonance (EPR) is a non-invasive analytical method that examines the resonant energy absorption of electrons in materials when exposed to microwave electromagnetic radiation. Through EPR spectroscopy, the unpaired electrons within materials can be detected. Typically, unpaired electrons are localized at defects, dangling bonds, or dopant centers. So, to further ascertain the presence of defects in Ni-doped CeO<sub>2</sub> (Ni/CeO<sub>2</sub>), the electron paramagnetic resonance (EPR) analysis was conducted at room temperature for pristine CeO<sub>2</sub> and Ni/CeO<sub>2</sub> samples with varying nickel content (1%, 5%, and 10%) (Fig. 3b and Fig. S5 ESI). Compared to pristine CeO<sub>2</sub>, Ni/CeO<sub>2</sub> exhibited EPR pattern with additional bands. The bands observed in the EPR spectra of CeO<sub>2</sub> and 1,5,10% Ni/CeO<sub>2</sub> at g values of 2.028, 2.028, 2.029 and 2.029, respectively, are attributed to the cubic sites of Ce<sup>3+</sup> or physisorbed oxygen molecules<sup>76</sup>. Additionally, the bands appearing at g values in the range 2.07-2.15 in Ni/CeO<sub>2</sub>, are attributed to the O<sup>2-</sup> species and Ce<sup>3+</sup>-O<sup>-</sup>-Ce<sup>4+</sup> defect sites<sup>77</sup>, which are absent in pristine CeO<sub>2</sub> (Fig. S5 ESI), confirming the enriched defects in Ni/CeO<sub>2</sub>. Collectively, the findings from PXRD, Raman spectroscopy, XPS, PL and EPR analyses confirm the increase in oxygen vacancy defects on doping CeO<sub>2</sub> with Ni and the oxygen vacancy defects in the doped CeO<sub>2</sub> increase on increasing the dopant, Ni concentration.

### 3.2 Morphological analysis

#### 3.2.1 FESEM and EDX analysis

To investigate the shapes and sizes, the synthesized Ni/CeO<sub>2</sub> was analyzed using a Field Emission Scanning Electron Microscope (FESEM). The FESEM image of Ni/CeO<sub>2</sub> depicted in (Fig. 4a) shows spherical morphology. It is found that the material is composed of Ce, Ni and O in desired amounts with no other impurities detected in the samples. The elemental mapping and chemical compositions of the Ni/CeO<sub>2</sub> studied by EDX are shown in Fig. 4b and 4c. Fig. 4b shows that cerium (Ce), nickel (Ni) and oxygen (O) are uniformly distributed. The EDX spectrum shows the presence of 73.72% cerium, 3.72% nickel, and 22.56 % oxygen, as detailed in the table (inset in Fig. 4c).



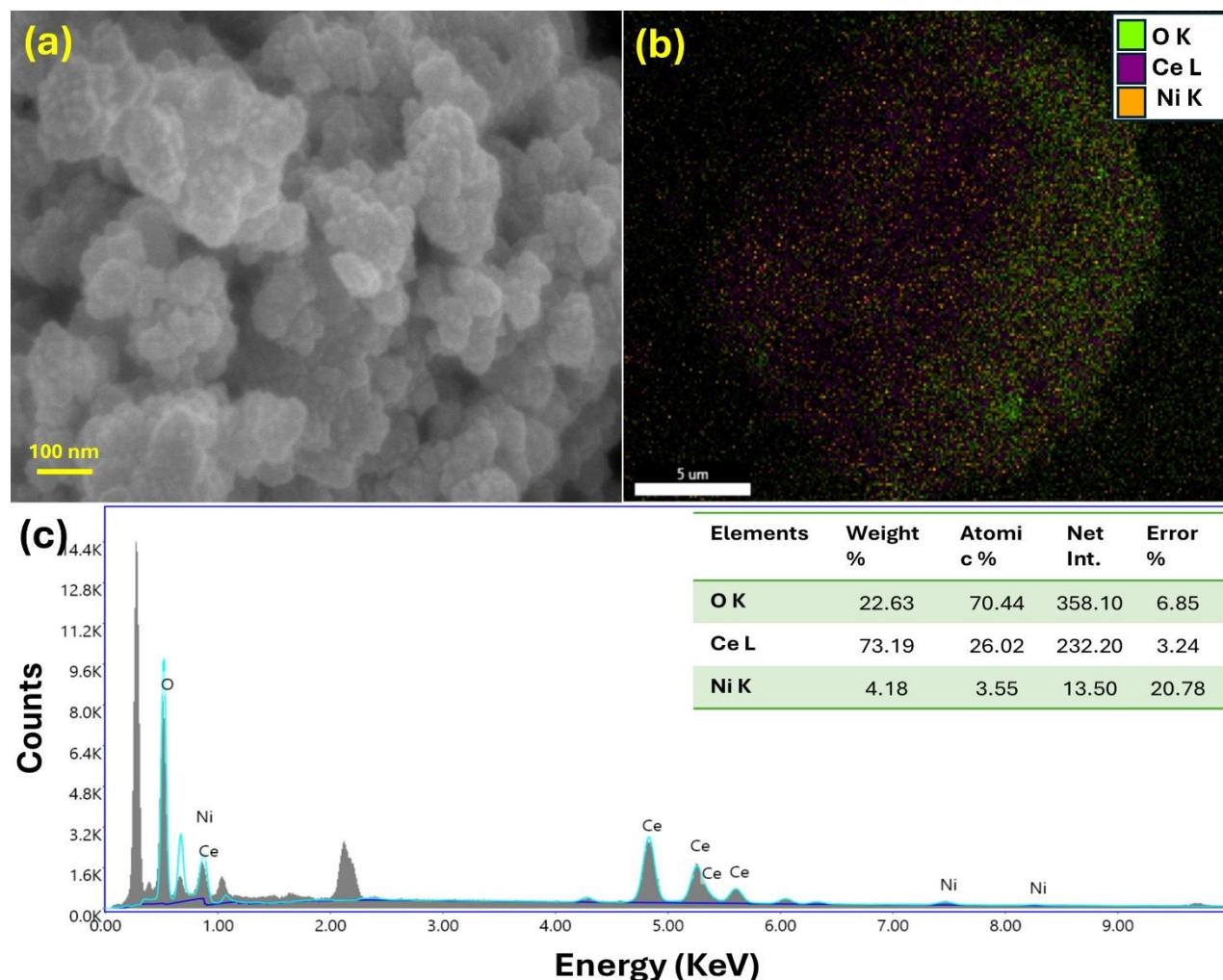


**Fig. 4** (a) FESEM image, (b) overlay of O + Ce + Ni and (c) EDX spectra and corresponding chemical composition analysis of Ni/CeO<sub>2</sub>.

### 3.2.2 HRTEM analysis

To study the microstructure of Ni-doped CeO<sub>2</sub>, High-Resolution Transmission Electron Microscopy (HRTEM) analysis was conducted. HRTEM images of pristine CeO<sub>2</sub> and Ni/CeO<sub>2</sub> particles are shown in Fig. 5a and Fig. S7a ESI. In the HRTEM image (Fig. 5b), the observed lattice fringe spacing of 0.312 nm corresponds to the (111) plane of CeO<sub>2</sub>, confirming the presence of a well-defined crystalline structure. Notably, no distinct lattice fringes attributable to nickel were detected, suggesting that the prepared material exists in a single-phase structure without separate nickel crystallites, and this observation matches with the result obtained from X-ray diffraction analysis, where no additional peak corresponding to Ni was observed. The selected area



electron diffraction (SAED) pattern of Ni/CeO<sub>2</sub>, shown in Fig. 5c, reveals the distinct ring pattern with bright dots. These patterns confirm the polycrystallinity of the synthesized nanomaterial. The d-values (interplanar spacings) for each ring from the large to the small ring in the SAED pattern for Ni/CeO<sub>2</sub> were calculated to verify the presence of cerium oxide. The calculated d-values, 0.311, 0.189, 0.156, and 0.123 nm, correspond to the crystal planes (111), (220), (222) and (331) of CeO<sub>2</sub>, respectively. The d-spacing values closely align with those calculated from the X-ray diffraction (XRD) pattern of the CeO<sub>2</sub>. The Ni/CeO<sub>2</sub> nanoparticles are estimated to be between 6-10 nm in size (Fig. S7b ESI), which is also in agreement with the values calculated from the X-ray diffraction (XRD) pattern.

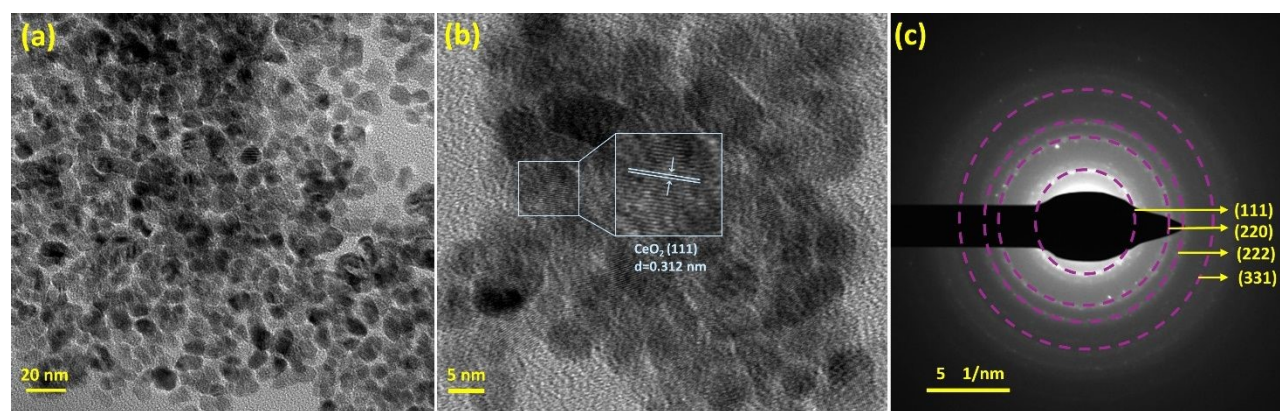


**Fig. 5** (a) Low-resolution TEM image, (b) HRTEM images with the lattice fringes, and (c) the selected area electron diffraction (SAED) sequence of Ni/CeO<sub>2</sub>.

### 3.3 X-ray photoelectron spectroscopy (XPS)

To evaluate the chemical composition, oxidation states and surface oxygen vacancies of the synthesized materials, X-ray photoelectron spectroscopic (XPS) analysis was carried out. In order to understand the effect of Ni on CeO<sub>2</sub>, XPS spectra of Ni/CeO<sub>2</sub> were compared with those of pristine CeO<sub>2</sub>. The XPS survey spectra of Ni/CeO<sub>2</sub> (Fig. 6a) confirm that the material consists of Ce, O, and Ni, with peaks in the binding energy ranges of 877-920 eV (Ce 3d), 527-535 eV (O 1s), and 840-890 eV (Ni 2p)<sup>78,48</sup>. The high-resolution data were calibrated using the C 1s signal at 284.5 eV as a reference<sup>79</sup>. To investigate the oxidation states of Ce, the high-resolution Ce 3d core XPS spectra in the range from 877 to 920 eV were deconvoluted and fitted.

The eight peaks present in XPS spectra of Ce 3d, labeled as V, V', V'', V''', U, U', U'' and U''' correspond to the binding energies (eV) 916.6, 906.3, 903.3, 900.8, 898.3, 888.3, 885.2, and 882.3



shown in Fig. 6b. These binding energy values of Ce 3d agree with the previously reported studies<sup>80,81</sup>. Among them, two peaks appearing at 882.3 eV (U''') and 903.3 eV (V'') correspond to Ce<sup>3+</sup> 3d<sub>5/2</sub> and Ce<sup>3+</sup> 3d<sub>3/2</sub>, whereas the other peaks at 898.3 eV (U) and 916.6 eV (V) are attributed to the Ce<sup>4+</sup> 3d<sub>5/2</sub> and Ce<sup>4+</sup> 3d<sub>3/2</sub>, respectively<sup>82</sup>. The presence of both Ce<sup>3+</sup> and Ce<sup>4+</sup> peaks in the Ce 3d spectra of CeO<sub>2</sub> confirms that these oxidation states coexist within the nanomaterial. The presence of Ce<sup>3+</sup> and Ce<sup>4+</sup> oxidation states causes the formation of defects, i.e., oxygen vacancies in the CeO<sub>2</sub> lattice, due to the interconversion between Ce<sup>3+</sup> and Ce<sup>4+</sup>.

The oxygen vacancy is commonly associated with the loss or migration of oxygen atoms, which plays an important role in catalytic reactions<sup>83,84</sup>. The formation of oxygen vacancies on the surface of ceria is influenced by the dopant. It was observed that Ni doping changes the concentration of oxygen vacancies in ceria. In the Ni/CeO<sub>2</sub> composite, the Ce 3d XPS spectra reveal a noticeable decrease in the Ce<sup>4+</sup> peak intensity along with a corresponding rise in Ce<sup>3+</sup> peak intensity compared to pristine CeO<sub>2</sub> (Fig. S4a and b ESI). This rise in the Ce<sup>3+</sup> peak intensity corresponds to an increase in oxygen vacancy in Ni/CeO<sub>2</sub>, which can be attributed to the incorporation of Ni into the CeO<sub>2</sub> lattice. The proportion of Ce<sup>3+</sup> can be quantified by calculating the ratio of the combined integrated areas of Ce<sup>3+</sup> peaks to the total integrated area of all peaks of Ce 3d in the form of the percentage of Ce<sup>3+</sup> (Eq. 4)<sup>85</sup> and is shown in Table S1 ESI<sup>86</sup>.

$$[\text{Ce}^{+3}] = \frac{(\text{Ce}^{+3})\text{Area}}{\sum(\text{Ce}^{+4} + \text{Ce}^{+3})\text{Area}} \times 100$$

The Ce<sup>3+</sup> content was found to be 25.17% and 14.39% for the Ni/CeO<sub>2</sub> and pristine CeO<sub>2</sub>, respectively (Table S1 ESI). The higher Ce<sup>3+</sup> content in Ni/CeO<sub>2</sub> compared to pristine CeO<sub>2</sub> suggests higher oxygen vacancies in Ni/CeO<sub>2</sub>, which can be attributed to the interfacial charge transfer between Ni and CeO<sub>2</sub>. To further ascertain the extent of oxygen vacancies in Ni/CeO<sub>2</sub>, the O 1s photoelectron spectra of Ni/CeO<sub>2</sub> and pristine CeO<sub>2</sub> (Fig. S4c and d ESI) were deconvoluted and compared. The main peaks around 529.9 eV and 532.1 eV (Fig. S4d ESI) correspond to lattice oxygen (O<sub>L</sub>) (Ce<sup>4+</sup>-O<sup>2-</sup>) and oxygen vacancy (O<sub>V</sub>) (Ce<sup>3+</sup>-O<sup>2-</sup>), respectively<sup>87</sup>. The intensities of the peak corresponding to oxygen vacancy are higher for Ni/CeO<sub>2</sub> compared to pristine CeO<sub>2</sub>, confirms enhancement of oxygen vacancies in Ni/CeO<sub>2</sub>. This result corroborates with the observation from Ce 3d peaks and agrees with the previous studies<sup>29,48</sup>. Additionally, the ratio of area under the peaks (O<sub>V</sub>/O<sub>L</sub>) corresponding to oxygen, O 1s in CeO<sub>2</sub> and Ni/CeO<sub>2</sub> were determined to be 0.6 and 1.9, respectively, as shown in Table S2 ESI. The higher O<sub>V</sub>/O<sub>L</sub> indicates a 3.1-fold increase in



oxygen vacancies in Ni/CeO<sub>2</sub>. Besides Ce, the presence of Ni is also ascertained from the peaks observed at 855.9 eV and 873.3 eV corresponding to Ni 2p<sub>3/2</sub> and Ni 2p<sub>1/2</sub>, respectively, while the peaks at 861.3 eV and 868.7 eV represent the satellite peaks, as illustrated in Fig. 6c. These observed peaks for Ni match with the reported literature<sup>88,89</sup>.

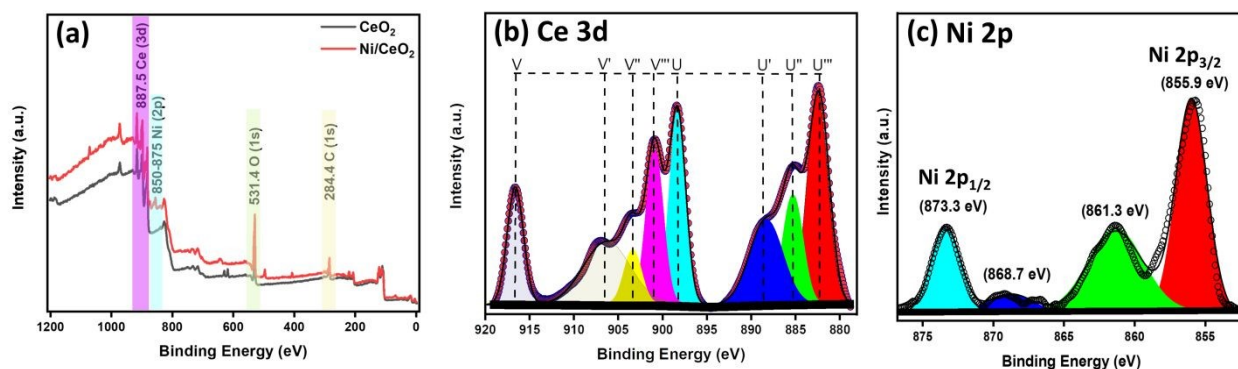


**Fig. 6** The XPS survey of CeO<sub>2</sub> and Ni/CeO<sub>2</sub> (a). Deconvoluted spectra of Ce 3d (b) and Ni 2p Ni/CeO<sub>2</sub> (c).

### 3.4 Surface area measurement

To study the surface properties of the materials, such as surface area, pore diameter, and pore volume, the Brunauer-Emmett-Teller (BET) measurement was conducted. Nitrogen adsorption-desorption isotherm (Fig. 7a) was used to analyse the surface area and pore size distribution of pristine CeO<sub>2</sub> and Ni/CeO<sub>2</sub>. From the isotherm, the porous feature of the materials is revealed from the steep increase in the curve at higher relative pressures. The pristine CeO<sub>2</sub> showed a surface area of 36.0 m<sup>2</sup>/g, a total pore volume of 0.15 cm<sup>3</sup>/g, and an average pore diameter of 7.5 nm. After the addition of Ni, the surface area increased to 39.9 m<sup>2</sup>/g, the pore volume increased to 0.21 cm<sup>3</sup>/g, and the pore diameter decreased to 5.4 nm. These changes in surface characteristics are attributed to the integration of Ni on CeO<sub>2</sub>. The improved surface features facilitate the electrocatalytic activity in Ni/CeO<sub>2</sub><sup>90</sup>.



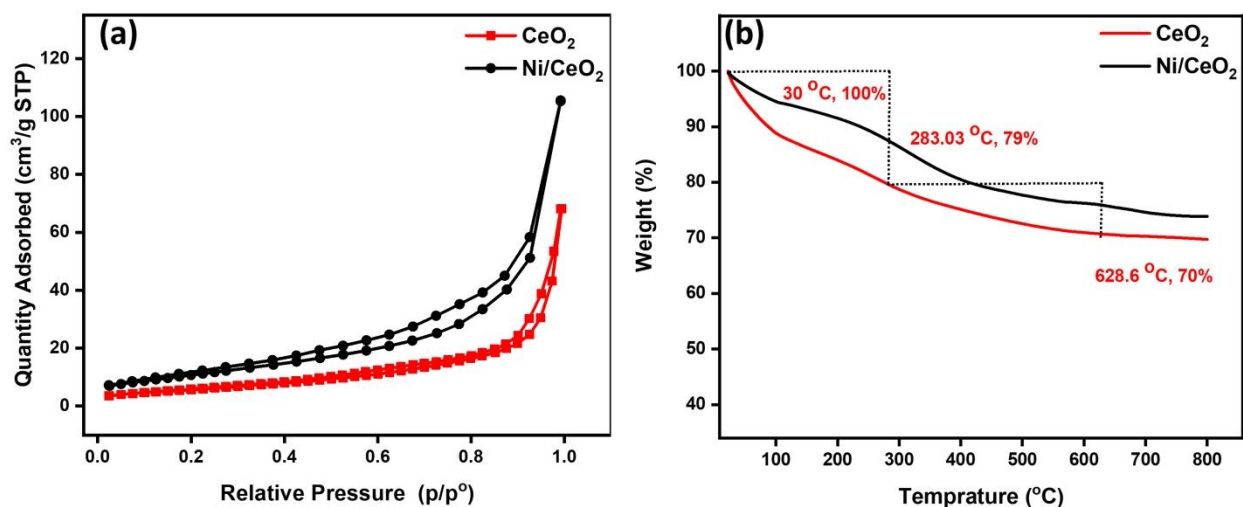


**Fig. 7** (a)  $N_2$  adsorption-desorption isotherms and (b) TGA analysis of  $CeO_2$  and  $Ni/CeO_2$ .

### 3.5 Thermal stability evaluation

Thermogravimetric analysis (TGA) was conducted between 30  $^{\circ}C$  and 800  $^{\circ}C$  at a heating rate of 10  $^{\circ}C/min$  to assess the thermal stability of both  $Ni/CeO_2$  and pristine  $CeO_2$ . The thermograms (Fig. 7b) reveal two phases of weight loss. The first phase shows a rapid 21% weight loss between 30  $^{\circ}C$  and 283.3  $^{\circ}C$ , attributable to the removal of water molecules physically adsorbed on the  $Ni/CeO_2$  surface (Fig. 7b). The second phase exhibits a 9% weight loss between 283.03  $^{\circ}C$  and 628.6  $^{\circ}C$ , likely due to the thermal decomposition of residual nitrate species originating from precursor salts and possible interactions involving  $Ni$  and  $Ce$  ions<sup>91</sup>. After 628.03  $^{\circ}C$ , the  $Ni/CeO_2$  catalyst shows minimal weight loss, indicating stability up to 800 $^{\circ}C$ . The weight losses were observed to be approximately 26% for  $Ni/CeO_2$  and 30% for  $CeO_2$ . Notably, pristine  $CeO_2$  loses more weight compared to the  $Ni/CeO_2$ , suggesting that the addition of  $Ni$  enhances the thermal stability of the electrocatalyst.

### 3.6. Oxygen Evolution Reaction:

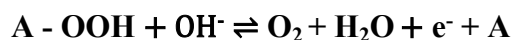
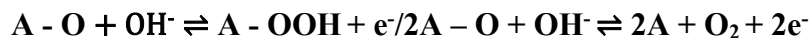
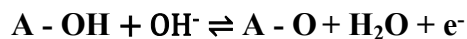
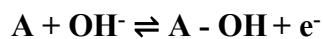
To evaluate the electrocatalytic performance of the materials and to understand the effect of incorporating  $Ni$  into  $CeO_2$ , electrodes of  $Ni$ -doped  $CeO_2$  ( $Ni/CeO_2$ ) and undoped  $CeO_2$  were used in the oxygen evolution reaction (OER). The electrocatalytic performance for the OER of the electrodes, including (Nickel Foam)  $NF$ ,  $NF/CeO_2$ ,  $NF/1\%Ni/CeO_2$ ,  $NF/5\%Ni/CeO_2$ , and  $NF/10\%Ni/CeO_2$ , was investigated in a 1M  $KOH$  solution using an  $Ag/AgCl$  and  $Pt$  as reference and



counter electrodes, respectively. The linear sweep voltammogram for the OER performance of NF, NF/CeO<sub>2</sub>, NF/1%Ni/CeO<sub>2</sub>, NF/5%Ni/CeO<sub>2</sub>, and NF/10%Ni/CeO<sub>2</sub> is shown in Fig. 8a. At a current density of 10 mA/cm<sup>2</sup>, the overpotentials for NF, NF/CeO<sub>2</sub>, NF/1%Ni/CeO<sub>2</sub>, NF/5%Ni/CeO<sub>2</sub>, and NF/10%Ni/CeO<sub>2</sub> were 442 mV, 406 mV, 384 mV, 357 mV, and 319 mV, respectively (as shown in Fig. 8b). There was a reduction in the overpotential when CeO<sub>2</sub> was incorporated in bare NF, confirming the catalytic role of CeO<sub>2</sub>. The overpotential value got further reduced with Ni/CeO<sub>2</sub> compared to undoped CeO<sub>2</sub>, indicating the effect of the dopant Ni. To understand the effect of the concentration of Ni, a varied amount of Ni was taken in Ni/CeO<sub>2</sub>. Notably, the overpotential got further reduced with an increase in Ni content in Ni/CeO<sub>2</sub>. There was a significant reduction in overpotential for the Ni/CeO<sub>2</sub> electrode with 10% Ni content compared to undoped CeO<sub>2</sub>. Similarly, the current density is also influenced significantly by an increase in Ni content in Ni/CeO<sub>2</sub>. Fig. 8c illustrates the current density for NF, NF/CeO<sub>2</sub>, NF/1%Ni/CeO<sub>2</sub>, NF/5%Ni/CeO<sub>2</sub>, and NF/10%Ni/CeO<sub>2</sub> at an applied potential of 2.4 V vs RHE. The corresponding values of the current densities were 78 mA/cm<sup>2</sup>, 100 mA/cm<sup>2</sup>, 104 mA/cm<sup>2</sup>, 115 mA/cm<sup>2</sup>, and 166 mA/cm<sup>2</sup>, respectively (as shown in Fig. 8c). The values of overpotential and current density show enhanced OER activity for Ni/CeO<sub>2</sub> compared to undoped CeO<sub>2</sub>. Incorporating CeO<sub>2</sub> onto NF enhanced the OER activity of NF/CeO<sub>2</sub> by reducing the overpotential by 36 mV and increasing the current density by 22 mA/cm<sup>2</sup>. The OER activity was further improved by incorporating Ni into CeO<sub>2</sub>. NF/1%Ni/CeO<sub>2</sub> exhibited an additional 22 mV reduction in overpotential and a 4 mA/cm<sup>2</sup> increase in current density compared to NF/CeO<sub>2</sub>. Interestingly, varying concentrations of Ni were also found to influence the electrocatalytic performance of the material. Further improvements were observed with increasing nickel content. NF/5%Ni/CeO<sub>2</sub> enhanced the OER performance, with a reduction in the overpotential by 27 mV and an increase in the current density by 11 mA/cm<sup>2</sup> compared to NF/1%Ni/CeO<sub>2</sub>. The best performance was observed for NF/10%Ni/CeO<sub>2</sub>, where the overpotential was significantly reduced by 38 mV, and the current density increased by 51 mA/cm<sup>2</sup> compared to NF/5%Ni/CeO<sub>2</sub>. Moreover, there was a remarkable decrease of 123 mV in the overpotential and a significant enhancement of 66 mA/cm<sup>2</sup> in the current density for NF/10%Ni/CeO<sub>2</sub> compared to the NF/CeO<sub>2</sub> (undoped CeO<sub>2</sub>). Fig. 8d represents the Tafel slope for OER for NF, NF/CeO<sub>2</sub>, NF/1%Ni/CeO<sub>2</sub>, NF/5%Ni/CeO<sub>2</sub>, and NF/10%Ni/CeO<sub>2</sub>, which were found to be 427 mV/dec, 381 mV/dec, 352 mV/dec, 286 mV/dec and 199 mV/dec, respectively. The Tafel slope, an important kinetic parameter that determines the overpotential necessary to



increase the current density, was significantly reduced by 48% with NF/10%Ni/CeO<sub>2</sub> compared to NF/CeO<sub>2</sub>. The reaction mechanism for the OER can be given by the equation below<sup>92</sup>;



Here, A represents the active site.

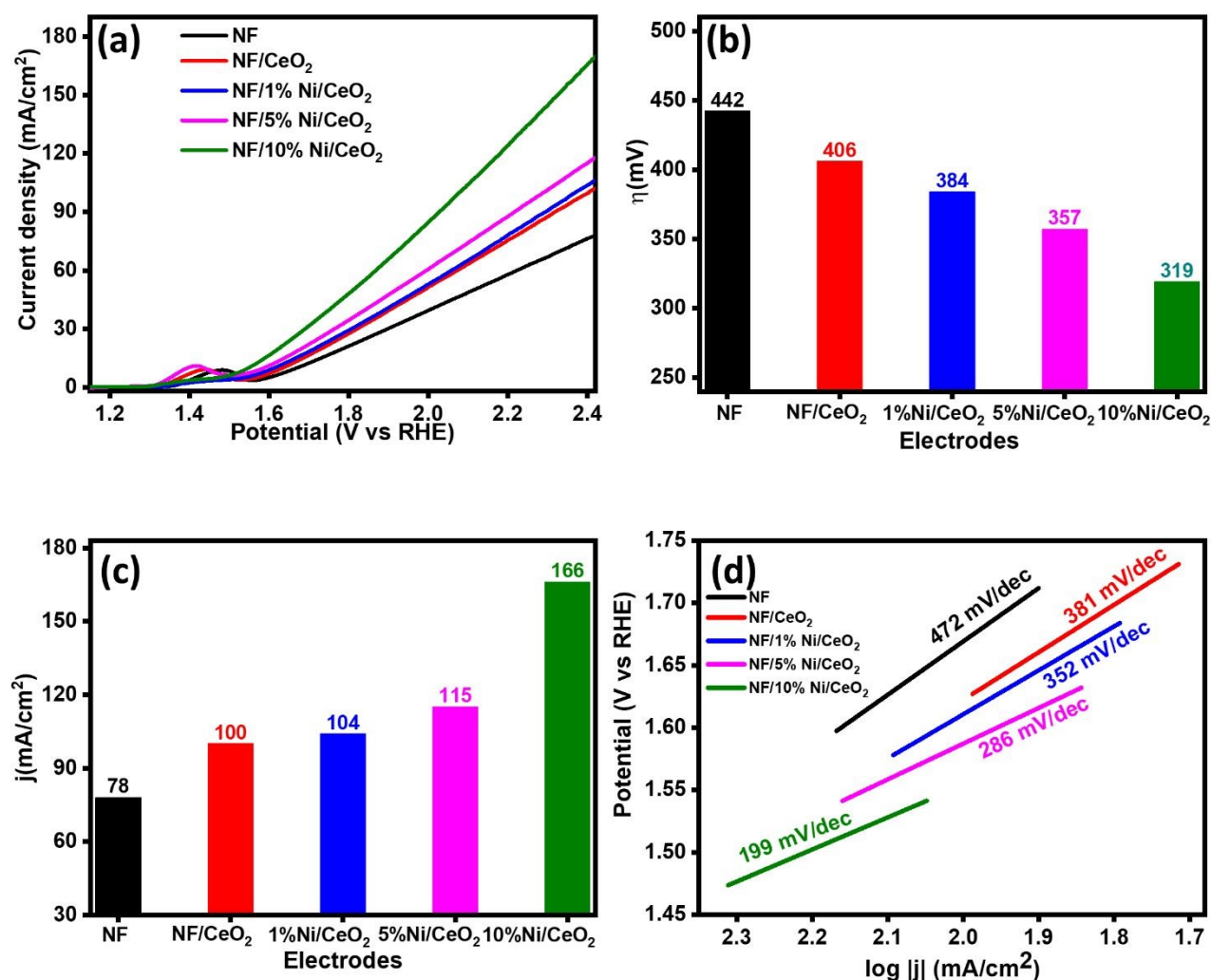


**Fig. 8** (a) LSV curves, (b) overpotential (vs. RHE) at a current density of 10 mA/cm<sup>2</sup>, (c) current density at a potential of 2.4 V, and (d) Tafel slope, for OER for NF, NF/CeO<sub>2</sub>, NF/1%Ni/CeO<sub>2</sub>, NF/5%Ni/CeO<sub>2</sub>, and NF/10%Ni/CeO<sub>2</sub>.



**Table 3:** Summary of OER performance with electrocatalysts.

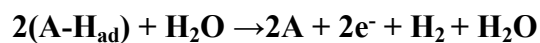
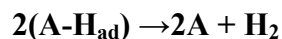
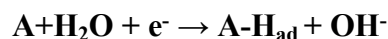
<b>Oxygen Evolution Reaction (OER)</b>			
<b>Electrocatalysts</b>	<b>Overpotential (mV) at 10 mA cm<sup>-2</sup></b>	<b>Current densities (mA cm<sup>-2</sup>)</b>	<b>Tafel slope (mV dec<sup>-1</sup>)</b>
NF	442	78	472
NF/CeO <sub>2</sub>	406	100	381
NF/1%Ni/CeO <sub>2</sub>	384	104	352
NF/5%Ni/CeO <sub>2</sub>	357	115	286
NF/10%Ni/CeO <sub>2</sub>	319	166	199

### 3.7. Hydrogen Evolution Reaction (HER)

After investigating the OER performance, the electrocatalytic activity for HER of the electrodes, including NF, NF/CeO<sub>2</sub>, NF/1%Ni/CeO<sub>2</sub>, NF/5%Ni/CeO<sub>2</sub>, and NF/10%Ni/CeO<sub>2</sub>, was also examined under the same experimental conditions. The LSV curves for the HER performance of NF, NF/CeO<sub>2</sub>, NF/1%Ni/CeO<sub>2</sub>, NF/5%Ni/CeO<sub>2</sub>, and NF/10%Ni/CeO<sub>2</sub>, are shown in Fig. 9a. The overpotentials calculated at a current density of 10 mA/cm<sup>2</sup> for NF, NF/CeO<sub>2</sub>, NF/1%Ni/CeO<sub>2</sub>, NF/5%Ni/CeO<sub>2</sub>, and NF/10%Ni/CeO<sub>2</sub>, were 418 mV, 271 mV, 263 mV, 228 mV, and 212 mV, respectively, as shown in Fig. 9b. It was observed that, there was a reduction in the overpotential with CeO<sub>2</sub> compared to bare NF proving the catalytic activity of CeO<sub>2</sub>. The overpotential got further reduced with Ni/CeO<sub>2</sub>, suggesting the improvement in catalytic activity on the introduction of dopant Ni in CeO<sub>2</sub>. It's worth noting that the overpotential got further reduced with Ni/CeO<sub>2</sub> on increasing Ni content. For NF/10%Ni/CeO<sub>2</sub>, there was a significant reduction in the overpotential compared to undoped CeO<sub>2</sub>. Similarly, the effect of Ni doping was found to be significant in the current density. Fig. 9c illustrates the current density at a potential of -0.6V for NF, NF/CeO<sub>2</sub>, NF/1%Ni/CeO<sub>2</sub>, NF/5%Ni/CeO<sub>2</sub>, and NF/10%Ni/CeO<sub>2</sub>. The values of current densities for NF, NF/CeO<sub>2</sub>, NF/1%Ni/CeO<sub>2</sub>, NF/5%Ni/CeO<sub>2</sub>, and NF/10%Ni/CeO<sub>2</sub>, were 22 mA/cm<sup>2</sup>, 40 mA/cm<sup>2</sup>, 45 mA/cm<sup>2</sup>, 64 mA/cm<sup>2</sup>, and 96 mA/cm<sup>2</sup>, respectively (as shown in Fig. 9c). The current density got increased with CeO<sub>2</sub> and the increase was more prominent with Ni/CeO<sub>2</sub> having 10% Ni content. The reduction in the overpotential and increase in the current density confirm the enhancement in the catalytic activity of the Ni/CeO<sub>2</sub> compared to undoped CeO<sub>2</sub>. The highest HER



performance was observed for NF/10%Ni/CeO<sub>2</sub>, where the overpotential decreased by 59 mV, and the current density increased significantly by 56 mA/cm<sup>2</sup> compared to undoped CeO<sub>2</sub>. Fig. 9d represents the Tafel slope (HER) for NF, NF/CeO<sub>2</sub>, NF/1%Ni/CeO<sub>2</sub>, NF/5%Ni/CeO<sub>2</sub>, and NF/10%Ni/CeO<sub>2</sub>. The values of Tafel slopes for NF, NF/CeO<sub>2</sub>, NF/1%Ni/CeO<sub>2</sub>, NF/5%Ni/CeO<sub>2</sub>, and NF/10%Ni/CeO<sub>2</sub> were found to be 432 mV/dec, 334 mV/dec, 306 mV/dec, 279 mV/dec, and 217 mV/dec, respectively. The Tafel slope got reduced by 215 mV/dec for NF/10%Ni/CeO<sub>2</sub> compared to bare NF, indicating improved charge transfer kinetics in Ni/CeO<sub>2</sub>. The best-performing electrode, NF/10%Ni/CeO<sub>2</sub>, exhibited the lowest overpotentials (319 mV for OER and 212 mV for HER) and the highest current densities (166 mA/cm<sup>2</sup> for OER and 96 mA/cm<sup>2</sup> for HER). These results demonstrate that the incorporation of Ni in CeO<sub>2</sub> and increasing Ni content significantly enhance the electrocatalytic performance of OER and HER. The reaction mechanism for HER can be given by the equations below<sup>93</sup>:



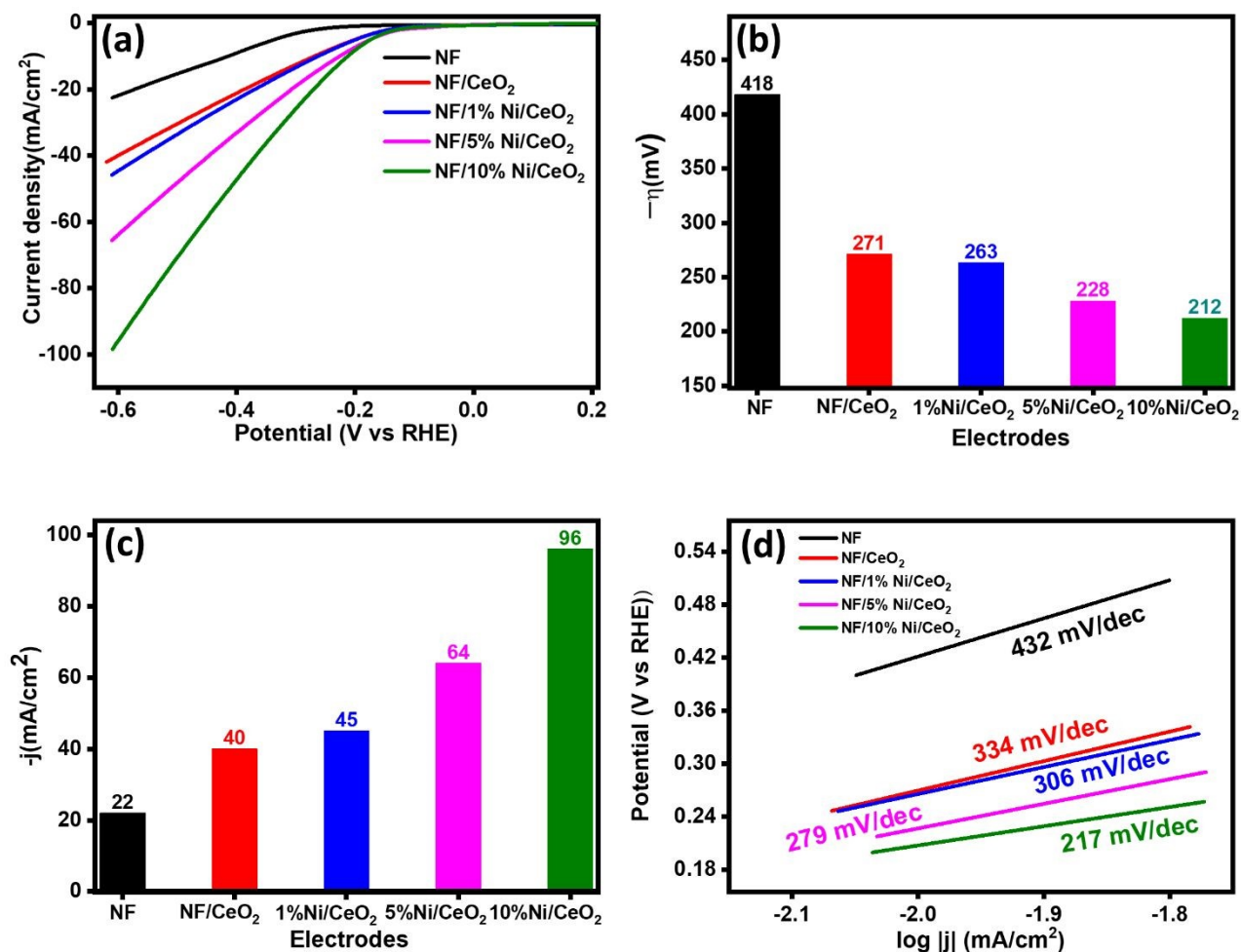


**Fig. 9** (a) LSV curves, (b) overpotential (vs. RHE) at a current density of 10 mA/cm<sup>2</sup>, (c) current density at a potential of -0.6 V, and (d) Tafel slope, for HER for NF, NF/CeO<sub>2</sub>, NF/1%Ni/CeO<sub>2</sub>, NF/5%Ni/CeO<sub>2</sub>, and NF/10%Ni/CeO<sub>2</sub>.

Furthermore, the stability of NF/10%Ni/CeO<sub>2</sub> was examined using chronoamperometric measurements over 45 minutes. The constant potential of 1.48 V (vs RHE) was applied to the electrode, and the corresponding current was plotted with respect to time. Fig. S6b ESI shows the chronoamperometric curves for NF/10%Ni/CeO<sub>2</sub>. For comparison, the chronoamperometric curve of NF/CeO<sub>2</sub> has also been provided.

**Table 4:** Summary of HER performance with the electrocatalysts.

Hydrogen Evolution Reaction (HER)
-----------------------------------



Electrocatalysts	Overpotential (mV) at 10 mA cm <sup>-2</sup>	Current densities (mA cm <sup>-2</sup> )	Tafel slope (mV dec <sup>-1</sup> )
NF	418	22	432
NF/CeO <sub>2</sub>	271	40	334
NF/1%Ni/CeO <sub>2</sub>	263	45	306
NF/5%Ni/CeO <sub>2</sub>	228	64	279
NF/10%Ni/CeO <sub>2</sub>	212	96	217

### 3.8. Electrochemical Stability and Gas Evolution Performance of Ni/CeO<sub>2</sub> Electrodes

The electrochemical durability of the NF/10%Ni/CeO<sub>2</sub> electrode was evaluated through chronoamperometric analysis over a period of 6 hours. During this test, a constant potential of 1.48 V (vs RHE) was maintained, and the variation in current density with time was continuously recorded. The corresponding chronoamperometric response (Fig. S6b ESI) reveals a stable current profile, indicating good operational stability of the electrode under prolonged anodic conditions.

Further, to assess the stability of oxygen vacancies before and after the electrochemical measurements, Raman spectroscopy was carried out on the Ni/CeO<sub>2</sub> electrode (Fig. S8). The electrode was fabricated via a drop-casting method using a catalyst (Ni/CeO<sub>2</sub>), polyvinylidene fluoride (PVDF), and carbon black in a weight ratio of 85:10:5, respectively. The Raman spectrum of Ni/CeO<sub>2</sub> displays a strong peak at approximately 457 cm<sup>-1</sup>, which corresponds to the F<sub>2g</sub> vibrational mode, a signature feature of the fluorite crystal structure of ceria. In addition, a broad defect-related band is observed in the range of ~560-660 cm<sup>-1</sup>, which is commonly attributed to oxygen vacancy-induced lattice distortions in CeO<sub>2</sub>. Importantly, post-electrocatalytic Raman analysis reveals that the intensity of this defect-associated band remains largely unchanged, with no noticeable decrease after the electrochemical study. This indicates that the oxygen vacancies are retained and are not significantly diminished during the electrocatalytic process. These observations demonstrate that the defect structure of ceria is robust with respect to electrocatalytic performance. In addition to stability assessment, the evolution of hydrogen (H<sub>2</sub>) and oxygen (O<sub>2</sub>) gases was quantitatively examined for the Ni-doped CeO<sub>2</sub> (Ni/CeO<sub>2</sub>) electrode using gas



quantification techniques. These measurements were conducted at the respective onset potentials associated with the hydrogen evolution reaction (HER) and oxygen evolution reaction (OER). For OER evaluation, a potential of 1.48 V (vs RHE) was applied, whereas HER measurements were performed at -0.6 V (vs RHE). The amounts of H<sub>2</sub> and O<sub>2</sub> generated were monitored over time intervals of 20, 40, 60, 80, 100, and 120 minutes, as illustrated in Fig. 10a and 10b. The obtained results demonstrate that the Ni/CeO<sub>2</sub> electrode is capable of sustained gas evolution for both HER and OER processes. The consistent production of gases over time highlights the catalytic activity of the material, while also suggesting that Ni incorporation into the CeO<sub>2</sub> lattice plays a significant role in enhancing OER performance.

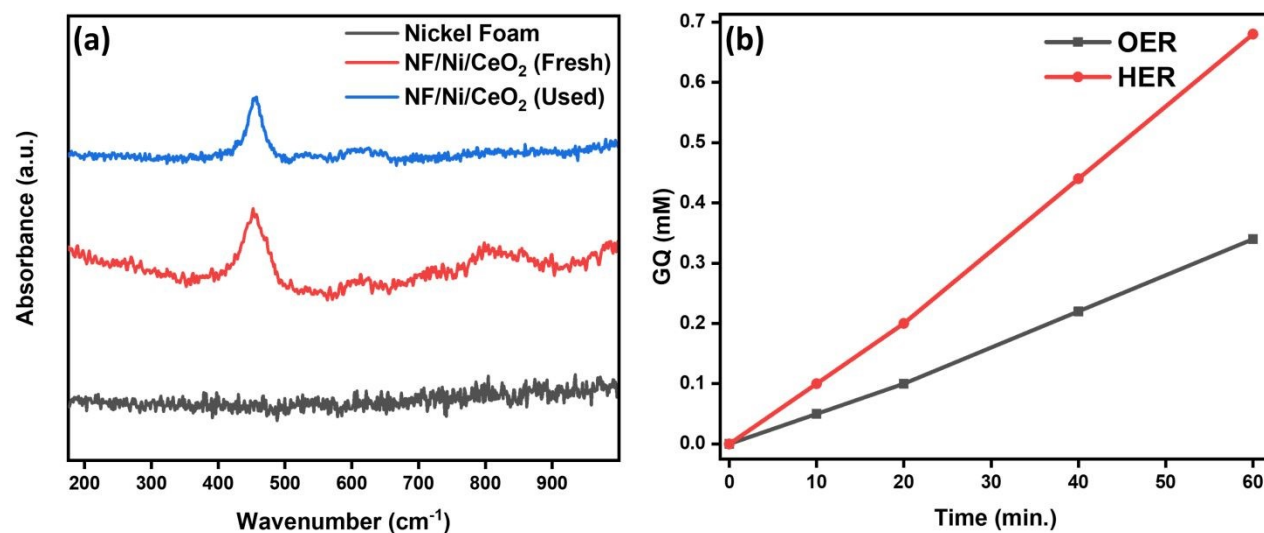


**Fig. 10** (a) Comparison study of Raman spectra of nickel foam and Ni/CeO<sub>2</sub> electrodes recorded before and after electrocatalytic performance, highlighting the preservation of the characteristic defect-induced bands associated with oxygen vacancies and (b) Evaluation of Faradaic efficiency for the Ni/CeO<sub>2</sub> electrode during hydrogen evolution reaction (HER) and oxygen evolution reaction (OER).



The Faradaic efficiency for hydrogen ( $F.E.H_2$ ) and oxygen ( $F.E.O_2$ ) was calculated following the equations<sup>94</sup>.

$$F.E.H_2 = \frac{V_{\text{experiment}}}{V_{\text{theoretical}}} = \frac{V_{\text{experiment}}}{\left(\frac{2}{4}\right)\left(\frac{Q}{F}\right)V_m} \dots\dots\dots(5)$$

$$F.E.O_2 = \frac{V_{\text{experiment}}}{V_{\text{theoretical}}} = \frac{V_{\text{experiment}}}{\left(\frac{2}{4}\right)\left(\frac{Q}{F}\right)V_m} \dots\dots\dots(6)$$

In these calculations, Q denotes the total charge, F is the Faraday constant, and Vm represents the molar volume of the gas.

The Ni/CeO<sub>2</sub> electrode exhibited high Faradaic efficiencies reached up to 95.1% for hydrogen evolution and around 90% for oxygen evolution. These values indicate efficient charge utilization and demonstrate a promising electrochemical performance of the electrode, with minimal energy losses during the conversion process.

#### 4.0. Proposed Mechanism for OER and HER

Based on the results of structural characterization and the electrocatalysis experiments, the enhancement in OER performance for the Ni-doped CeO<sub>2</sub> electrode, NF/10%Ni/CeO<sub>2</sub>, can be attributed to the increased concentration of oxygen vacancies due to the interaction of Ni and CeO<sub>2</sub>. Ni doped in CeO<sub>2</sub> enhanced the oxygen vacancies, which are crucial in improving electrocatalytic performance (Fig.11). A higher concentration of oxygen vacancies leads to an increase in active sites, thereby accelerating the OER process and reducing the required overpotential. Additionally, the incorporation of Ni induces the enhancement of spin-triplet O<sub>2</sub>, which facilitates electron transfer by modulating the spin states, reducing spin-state energy barriers, and further improving reaction kinetics. On the other hand, for NF/CeO<sub>2</sub> and NF/1%Ni/CeO<sub>2</sub>, the enhancement in performance was relatively modest, as the lower Ni content resulted in fewer defects, i.e. oxygen vacancies. With only 1% Ni incorporation, the number of oxygen vacancies was not sufficient to induce a significant catalytic improvement, which is evident from the smaller reduction in overpotential and the slight increase in current density. This observation is further supported by X-ray Photoelectron Spectroscopy (XPS) and other structural characterizations, which confirm



that oxygen vacancy formation is more pronounced at higher Ni concentrations. Similarly, the enhanced HER performance observed for NF/10%Ni/CeO<sub>2</sub> can be attributed to the lower charge transfer resistance ( $R_{ct}$ ), as confirmed by EIS measurements (Fig. S6a ESI). A lower  $R_{ct}$  signifies improved electron transport at the electrode-electrolyte interface, facilitating faster charge transfer and reducing the energy barrier for the HER process. The increased Ni content in CeO<sub>2</sub> enhances electrical conductivity and provides more active sites, which effectively reduces the impedance, allowing for efficient charge transport. This reduction in charge transfer resistance further justifies the significant decrease in overpotential and the increase in current density observed for NF/10%Ni/CeO<sub>2</sub>.

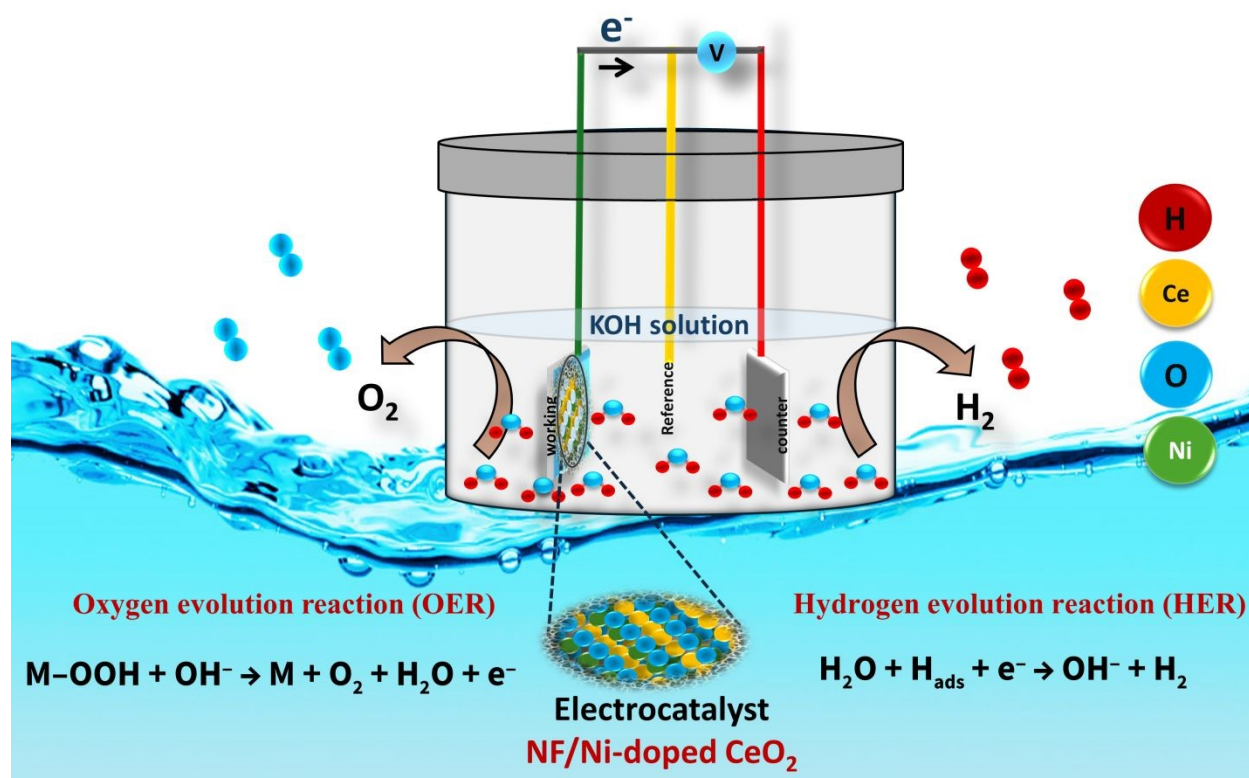


**Fig. 11** Mechanism of the electrocatalytic water splitting.

**Table 5:** Comparison of overpotential values for HER and OER at a current density of 10 mA/cm<sup>2</sup> in 1M KOH solution, as reported in the literature, for different CeO<sub>2</sub>-based catalysts.

Electrocatalysts	Reaction	Overpotential (mV) @ 10 mA/cm <sup>2</sup>	Ref.
Ni/Ceria	HER	588	95



Ni/Ceria-rGO	HER	208	52
CeO <sub>2</sub> /Ni/NC	HER	320	96
<b>NF/10%Ni/CeO<sub>2</sub></b>	<b>HER</b>	<b>212</b>	<b>This work</b>
Ce-NiO-E	OER	382	97
(Ni-Fe-Co-Ce) O <sub>x</sub>	OER	410	98
Ni-Ce/NC	OER	530	99
CeO <sub>2</sub> /Ni/NC	OER	390	64
20%Ni+Fe-CeO <sub>2</sub>	OER	380	100
<b>NF/10% Ni/CeO<sub>2</sub></b>	<b>OER</b>	<b>319</b>	<b>This work</b>

## 5.0. CONCLUSIONS

In the quest for an efficient electrocatalyst, this study reports the design of ceria-based materials for the evolution of hydrogen and oxygen by electrocatalytic water splitting. While attaining significant improvement in electrocatalytic performance for nickel-doped ceria (Ni/CeO<sub>2</sub>), it demonstrates how the increase in concentration of dopant increases oxygen vacancy defect in ceria, and an increase in defect in ceria enhances the electrocatalytic performance of Ni/CeO<sub>2</sub>. We reported the preparation of Ni/CeO<sub>2</sub> that produced oxygen vacancy defects in ceria. Compared to pristine CeO<sub>2</sub>, higher oxygen vacancies in Ni/CeO<sub>2</sub> confirmed the effect of the incorporation of Ni in CeO<sub>2</sub>. Dopant concentration-dependent oxygen vacancy generation was ascertained. Generation of oxygen vacancies was verified by Raman spectroscopy, XPS, photoluminescence and EPR studies. Oxygen vacancies in Ni/CeO<sub>2</sub> were quantified by Raman spectroscopy studies. Detailed structural insights were derived from XRD, Raman, XPS, EDX, FESEM and HRTEM analysis. Stability of the catalyst was evaluated by TGA and Chronoamperometry. Ni/CeO<sub>2</sub> was evaluated to be an effective electrocatalyst for the evolution of hydrogen and oxygen by water splitting, using linear sweep voltammetry. A significant reduction in overpotentials by 87 mV for oxygen evolution and 59 mV for hydrogen evolution was observed for Ni/CeO<sub>2</sub> compared to pristine CeO<sub>2</sub>. Besides, there was a notable increase in current densities by 166 mA/cm<sup>2</sup> for oxygen evolution and 96 mA/cm<sup>2</sup> for hydrogen evolution. Also, the faster reaction kinetics were observed from the reduction in Tafel slope from 381 to 199 mV/dec for OER and from 334 to 217 mV/dec for HER. Electrochemical impedance spectroscopy (EIS) analysis revealed that the Ni/CeO<sub>2</sub> electrocatalyst exhibited the lowest charge transfer resistance, indicating enhanced interfacial charge transport



and superior electrocatalytic activity. The electrocatalytic performance of Ni/CeO<sub>2</sub> was found to be affected by the increase in concentration of dopant. Ni/CeO<sub>2</sub> with 10% nickel exhibited optimal performance, with substantial reductions in overpotential and a marked increase in current density with improved charge carrier dynamics. The enhanced electrocatalytic performance was attributed to the incorporation of Ni into ceria causing; (i) increased oxygen vacancy defects in Ni/CeO<sub>2</sub>, (ii) enhancement of spin-triplet O<sub>2</sub>, (iii) low charge transfer resistance (R<sub>ct</sub>) facilitating electron transport at the electrode-electrolyte interface, (iv) enhancement in electrical conductivity and (v) reduction in impedance. This study concluded the synergistic interaction between Ni and CeO<sub>2</sub>, defining the critical role of dopant concentration for modulating oxygen vacancy, which results in designing efficient water-splitting catalysts.

## ASSOCIATED CONTENT\*

### Supporting Information

UV-vis absorption spectra, powder XRD peak, Raman peak shifting and intensity variation, XPS spectra of CeO<sub>2</sub>, calculation of Ce<sup>3+</sup> content from Ce 3d XPS spectra, Oxygen vacancy calculation from O 1s in XPS spectra, O 1s XPS spectra, EPR spectra, electrocatalytic performance, TEM image of CeO<sub>2</sub> and average particle size of Ni/CeO<sub>2</sub>.

## AUTHOR INFORMATION

### Corresponding Author

**Nityananda Agasti** -Department of Chemistry, University of Delhi, Delhi, 110007, India. <https://orcid.org/0000-0003-1934-907X>

Email: [mnagasti@chemistry.du.ac.in](mailto:mnagasti@chemistry.du.ac.in)

### Notes

The authors declare no competing financial interest.

### Acknowledgement

NA acknowledges the grant, Ref. No./IoE/2025-26/12/FRP under the Faculty Research



Programme from the Institute of Eminence, University of Delhi. Ajit Kumar Dhanka thanks the Council of Scientific & Industrial Research (CSIR) and the University Grants Commission (UGC) for Junior Research Fellowship (JRF)-16-6(119119 Dec. 2018/19). Authors would also like to acknowledge University Science Instrumentation Centre (USIC) and Department of Physics & Astrophysics, University of Delhi, Special Centre for Nanoscience, Jawaharlal Nehru University (JNU), New Delhi, Central Research Facility (CRF), Indian Institute of Technology (IIT) Delhi, New Delhi, India, for the characterization facilities. The TEM facilities at the Sophisticated Analytical Instrumentation Facility (SAIF) at All India Institute of Medical Sciences (AIIMS), New Delhi, are gratefully acknowledged for the HRTEM measurements.

## References

1. Hojjati-Najafabadi, A., Behmadi, R., He, Y., Kamyab, H., & Vasseghian, Y. (2025). Tailoring high-entropy alloys for cutting-edge hydrogen evolution electrocatalysis. *Sustainable Materials and Technologies*, e01655. <https://doi.org/10.1016/j.susmat.2025.e01655>
2. Wang, J., & Azam, W. (2024). Natural resource scarcity, fossil fuel energy consumption, and total greenhouse gas emissions in top emitting countries. *Geoscience frontiers*, 15(2), 101757. <https://doi.org/10.1016/j.gsf.2023.101757>
3. Dale, S. (2021). BP statistical review of world energy. *BP Plc: London, UK*, 14-16. <https://www.bp.com/content/dam/bp/business-sites/en/global/corporate/pdfs/energy-economics/statistical-review/bp-stats-review-2021-full-report.pdf>
4. Rosyid, F. A., & Adachi, T. (2016). Coal mining in Indonesia: forecasting by the growth curve method: Rosyid FA, Adachi T. *Mineral Economics*, 29(2), 71-85. <https://doi.org/10.1007/s13563-016-0091-6>
5. Khaleel, M., Yusupov, Z., Ahmed, A., Alsharif, A., Nassar, Y., & El-Khozondar, H. (2023). Towards sustainable renewable energy. *Applied solar energy*, 59(4), 557-567. <https://doi.org/10.3103/S0003701X23600704>
6. Wu, J., He, Y., Behmadi, R., Hojati, N., Xu, L., Li, C., & Hojjati-Najafabadi, A. (2026). High-performance self-supporting FeCoNiCrMo HEA catalyst for alkaline hydrogen evolution. *Journal of Power Sources*, 669, 239383. <https://doi.org/10.1016/j.jpowsour.2026.239383>
7. Xu, L., Wu, S., He, X., Wang, H., Deng, D., Wu, J., & Li, H. (2022). Interface engineering of anti-perovskite Ni<sub>3</sub>FeN/VN heterostructure for high-performance rechargeable zinc–air batteries. *Chemical Engineering Journal*, 437, 135291. <https://doi.org/10.1016/j.cej.2022.135291>
8. Saha, P., Akash, F. A., Shovon, S. M., Monir, M. U., Ahmed, M. T., Khan, M. F. H., & Akter, R. (2024). Grey, blue, and green hydrogen: A comprehensive review of production methods and prospects for zero-emission energy. *International Journal of Green Energy*, 21(6), 1383-1397. <https://doi.org/10.1080/15435075.2023.2244583>
9. Kaiwen, L., Bin, Y., & Tao, Z. (2018). Economic analysis of hydrogen production from steam reforming process: A literature review. *Energy Sources, Part B: Economics, Planning, and Policy*, 13(2), 109-115. <https://doi.org/10.1080/15567249.2017.1387619>



10. Caballero, J. J. B., Zaini, I. N., & Yang, W. (2022). Reforming processes for syngas production: A mini-review on the current status, challenges, and prospects for biomass conversion to fuels. *Applications in Energy and Combustion Science*, 10, 100064. <https://doi.org/10.1016/j.jaecs.2022.100064>
11. Chen, L., Qi, Z., Zhang, S., Su, J., & Somorjai, G. A. (2020). Catalytic hydrogen production from methane: A review on recent progress and prospect. *Catalysts*, 10(8), 858. <https://doi.org/10.3390/catal10080858>
12. Kumar, R., Singh, R., & Dutta, S. (2024). Review and outlook of hydrogen production through catalytic processes. *Energy & Fuels*, 38(4), 2601-2629. <https://doi.org/10.1021/acs.energyfuels.3c04026>
13. Hojjati-Najafabadi, A., Heidari, G., Afsharpour, M., Belver, C., Aminabhavi, T. M., Vasseghian, Y., & He, Y. (2025). Dual-functional hierarchical NiFe hydroxylphosphate electrocatalyst on copper dendrites for hydrogen and oxygen evolution. *Chemical Engineering Journal*, 518, 164622. <https://doi.org/10.1016/j.cej.2025.164622>
14. Feng, J. X., Ye, S. H., Xu, H., Tong, Y. X., & Li, G. R. (2016). Design and synthesis of FeOOH/CeO<sub>2</sub> heterolayered nanotube electrocatalysts for the oxygen evolution reaction. *Advanced Materials*, 28(23), 4698-4703. <https://doi.org/10.1002/adma.201600054>
15. Li, T., Li, S., Liu, Q., Tian, Y., Zhang, Y., Fu, G., & Tang, Y. (2019). Hollow Co<sub>3</sub>O<sub>4</sub>/CeO<sub>2</sub> heterostructures in situ embedded in N-doped carbon nanofibers enable outstanding oxygen evolution. *ACS Sustainable Chemistry & Engineering*, 7(21), 17950-17957. <https://doi.org/10.1021/acssuschemeng.9b04699>
16. He, Y., Tan, R., Li, L., Behmadi, R., Sun, S., Zhu, C., & Hojjati-Najafabadi, A. (2026). Electrospinning-Derived FeCrNiZrMn High-Entropy Alloy on Carbon Nanofibers for Hydrogen Evolution. *ChemCatChem*, 18(3), e01811. <https://doi.org/10.1002/cctc.202501811>
17. Li, X., Wang, Z., & Wang, L. (2021). Metal-organic framework-based materials for solar water splitting. *Small Science*, 1(5), 2000074. <https://doi.org/10.1002/ssm.202000074>
18. Mishra, K., Devi, N., Siwal, S. S., Gupta, V. K., & Thakur, V. K. (2023). Hybrid semiconductor photocatalyst nanomaterials for energy and environmental applications: fundamentals, designing, and prospects. *Advanced Sustainable Systems*, 7(8), 2300095. <https://doi.org/10.1002/adsu.202300095>
19. Li, S., Zhang, X., Yang, F., Zhang, J., Shi, W., & Rosei, F. (2024). Mechanically driven water splitting over piezoelectric nanomaterials. *Chem Catalysis*, 4(2). <https://doi.org/10.1016/j.checat.2024.100901>
20. Tigwere, G. A., Khan, M. D., Nyamen, L. D., de Souza, F. M., Lin, W., Gupta, R. K., & Ndifon, P. T. (2023). Transition metal (Ni, Cu and Fe) doped MnS nanostructures: effect of doping on supercapacitance and water splitting. *Materials Science in Semiconductor Processing*, 158, 107365. <https://doi.org/10.1016/j.mssp.2023.107365>
21. Liu, D., & Kuang, Y. (2024). Yashwanth, H. J., Hareesh, K., Rondiya, S. R., Choudhary, R. J., & Dhole, S. D. (2024). The borophene quantum dots scaffolded TiO<sub>2</sub> nanocomposite as an efficient photo electrocatalyst for water splitting application. *Applied Surface Science*, 646, 158910. <https://doi.org/10.1016/j.apsusc.2023.158910>
22. Mehtab, A., Alshehri, S. M., & Ahmad, T. (2022). Photocatalytic and photoelectrocatalytic water splitting by porous g-C<sub>3</sub>N<sub>4</sub> nanosheets for hydrogen generation. *ACS Applied Nano Materials*, 5(9), 12656-12665. <https://doi.org/10.1021/acsnm.2c02460>



23. Mohan, H., & Shin, T. (2025). Enhanced photocatalytic water-splitting performance of Fe/CdS nanomaterials: Structural, optical, and electrochemical insights. *Materials Science in Semiconductor Processing*, 199, 109892. <https://doi.org/10.1016/j.mssp.2025.109892>
24. Li, D. J., Gu, Z. G., Zhang, W., Kang, Y., & Zhang, J. (2017). Epitaxial encapsulation of homodispersed CeO<sub>2</sub> in a cobalt–porphyrin network derived thin film for the highly efficient oxygen evolution reaction. *Journal of Materials Chemistry A*, 5(38), 20126–20130. <https://doi.org/10.1039/C7TA06580A>
25. Sivanantham, A., Ganesan, P., & Shanmugam, S. (2018). A synergistic effect of Co and CeO<sub>2</sub> in nitrogen-doped carbon nanostructure for the enhanced oxygen electrode activity and stability. *Applied Catalysis B: Environmental*, 237, 1148–1159. <https://doi.org/10.1016/j.apcatb.2017.08.063>
26. Ghemit, K., Akika, F. Z., Rouibah, K., Benamira, M., Bousba, D., Gouasmia, A., & Avramova, I. (2025). Photocatalytic activity of the new NiAl<sub>2</sub>O<sub>4</sub>/CeO<sub>2</sub> heterojunction for the elimination of Rose Bengal under solar irradiation. *Inorganic Chemistry Communications*, 176, 114185. <https://doi.org/10.1016/j.inoche.2025.114185>
27. Krishnan, A., Archana, K., Arsha, A. S., Viswam, A., & Meera, M. S. (2025). Divulging the potential role of wide band gap semiconductors in electro and photo catalytic water splitting for green hydrogen production. *Chinese Journal of Catalysis*, 68, 103–154. [https://doi.org/10.1016/S1872-2067\(24\)60156-7](https://doi.org/10.1016/S1872-2067(24)60156-7)
28. Mazloom, J., Ghodsi, F. E., Tepehan, F. Z., Tepehan, G. G., & Turhan, I. (2018). Enhanced lithium electrochemical performance and optical properties of CeO<sub>2</sub>–SnO<sub>2</sub> nanocomposite thin films by transition metal (TM: Ni, Mn, and Co) doping. *Journal of Sol-Gel Science and Technology*, 86, 51–62. <https://doi.org/10.1007/s10971-018-4603-4>
29. Bôas, N. V., Junior, J. B. S., Varanda, L. C., Machado, S. A. S., & Calegari, M. L. (2019). Bismuth and cerium doped cryptomelane-type manganese dioxide nanorods as bifunctional catalysts for rechargeable alkaline metal-air batteries. *Applied Catalysis B: Environmental*, 258, 118014. <https://doi.org/10.1016/j.apcatb.2019.118014>
- <sup>30</sup>. Dai, S., Montero-Lanzuela, E., Tissot, A., Baldoví, H. G., García, H., Navalón, S., & Serre, C. (2023). Room temperature design of Ce (IV)-MOFs: from photocatalytic HER and OER to overall water splitting under simulated sunlight irradiation. *Chemical Science*, 14(13), 3451–3461. <https://doi.org/10.1039/D2SC05161C>
31. Ghosh, S., Pal, S., Biswas, M., Thandavarayan, M., Reddy, A. A., & Naskar, M. K. (2024). Dual Active Site Mediated Photocatalytic H<sub>2</sub> Evolution through Water Splitting Using CeO<sub>2</sub>/PPy/BFO Double Heterojunction Catalyst. *ACS Applied Energy Materials*. <https://doi.org/10.1021/acsaem.4c00269>
32. Dhanka, A. K., Tiwari, M., Bhartiya, P. K., Pani, B., Agasti, N., & Mishra, D. (2025). Oxygen vacancies induced low overpotentials of Ag/CeO<sub>2</sub> for electrocatalytic evolution of oxygen and hydrogen. *Materials Advances*, 6(11), 3716–3729. <https://doi.org/10.1039/D5MA00321K>
33. Liu, G., Wang, M., Wu, Y., Li, N., Zhao, F., Zhao, Q., & Li, J. (2020). 3D porous network heterostructure NiCe@NiFe electrocatalyst for efficient oxygen evolution reaction at large current densities. *Applied Catalysis B: Environmental*, 260, 118199. <https://doi.org/10.1016/j.apcatb.2019.118199>
34. Song, J., Wei, C., Huang, Z. F., Liu, C., Zeng, L., Wang, X., & Xu, Z. J. (2020). A review on fundamentals for designing oxygen evolution electrocatalysts. *Chemical Society Reviews*, 49(7), 2196–2214. <https://doi.org/10.1039/C9CS00607A>
35. Demir, E., Akbayrak, S., Önal, A. M., & Özkar, S. (2019). Ceria supported ruthenium (0) nanoparticles: Highly



efficient catalysts in oxygen evolution reaction. *Journal of colloid and interface science*, 534, 704-710. <https://doi.org/10.1016/j.jcis.2018.09.07>

36. Jiang, S., Zhang, R., Liu, H., Rao, Y., Yu, Y., Chen, S., & Kang, Y. (2020). Promoting formation of oxygen vacancies in two-dimensional cobalt-doped ceria nanosheets for efficient hydrogen evolution. *Journal of the American Chemical Society*, 142(14), 6461-6466. <https://dx.doi.org/10.1021/jacs.9b13915>

37. He, Y., Wu, J., Hu, F., Mao, L., Aminabhavi, T. M., Vasseghian, Y., & Hojjati-Najafabadi, A. (2024). Self-supporting FeCoNiCuTiGa high-entropy alloy electrodes for alkaline hydrogen and oxygen evolution reactions: experimental and theoretical insights. *ACS Applied Energy Materials*, 7(20), 9121-9133. <https://doi.org/10.1021/acsam.4c01036>

38. Selvanathan, S., Woi, P. M., & Srivastava, R. (2023). Transition metal-based single-atom catalyst for photoelectrochemical water splitting. In *Solar-Driven Green Hydrogen Generation and Storage* (pp. 61-85). Elsevier. <https://doi.org/10.1016/B978-0-323-99580-1.00001-7>

39. Yang, Z., Zheng, D., Yue, X., Wang, K., Hou, Y., Dai, W., & Fu, X. (2023). The synergy of Ni doping and oxygen vacancies over CeO<sub>2</sub> in visible light-assisted thermal catalytic methanation reaction. *Applied Surface Science*, 615, 156311. <https://doi.org/10.1016/j.apsusc.2022.156311>

40. Mishra, P. K., Acharya, S., Palai, A., Sahu, S. K., Meher, A., & Sahu, D. (2024). Strategic Ni integration to study its impact on the photoluminescence and photocatalytic performances of SnO<sub>2</sub> nanorod architecture. *Chemistry of Inorganic Materials*, 3, 100055. <https://doi.org/10.1016/j.cinorg.2024.100055>

41. Zhang, Y., Guo, P., Li, S., Sun, J., Wang, W., Song, B., & Xu, P. (2022). Magnetic field assisted electrocatalytic oxygen evolution reaction of nickel-based materials. *Journal of Materials Chemistry A*, 10(4), 1760-1767. <https://doi.org/10.1039/D1TA09444K>

42. Sun, T., Tang, Z., Zang, W., Li, Z., Li, J., Li, Z., & Lu, J. (2023). Ferromagnetic single-atom spin catalyst for boosting water splitting. *Nature Nanotechnology*, 18(7), 763-771. <https://doi.org/10.1038/s41565-023-01407-1>

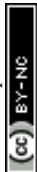
43. Tiwari, M., & Mishra, D. (2024). Enhanced spin-polarization and detection limit in a spin-based optoelectrochemical DNA hybridization sensor induced by circularly polarized light. *Sensors & Diagnostics*, 3(7), 1159-1166. <https://doi.org/10.1039/D4SD00109E>

44. Oliveira, F. A. C., Barreiros, M. A., Haeussler, A., Caetano, A. P., Mouquinho, A. I., e Silva, P. M. O., & Abanades, S. (2020). High performance cork-templated ceria for solar thermochemical hydrogen production via two-step water-splitting cycles. *Sustainable Energy & Fuels*, 4(6), 3077-3089. <https://doi.org/10.1039/D0SE00318B>

45. Koyale, P. A., Mulik, S. V., Gunjekar, J. L., Dongale, T. D., Koli, V. B., Mullani, N. B., & Delekar, S. D. (2024). Synergistic enhancement of water-splitting performance using mof-derived ceria-modified g-C<sub>3</sub>N<sub>4</sub> nanocomposites: Synthesis, performance evaluation, and stability prediction with machine learning. *Langmuir*, 40(26), 13657-13668. <https://doi.org/10.1021/acs.langmuir.4c01336>

46. Orfila, M., Sanz, D., Linares, M., Molina, R., Sanz, R., Marugán, J., & Botas, J. Á. (2021). H<sub>2</sub> production by thermochemical water splitting with reticulated porous structures of ceria-based mixed oxide materials. *International Journal of Hydrogen Energy*, 46(33), 17458-17471. <https://doi.org/10.1016/j.ijhydene.2020.04.222>

47. Yan, K., Wen, C., Li, R., Zhang, B., Liu, T., Liu, Q., & Zhou, Z. (2023). Morphological optimized CeO<sub>2</sub> and Cu-doped CeO<sub>2</sub> nanocrystals for hydrogen production by solar photo-thermochemical water splitting based on surface



photoinduced oxygen vacancies. *Applied Surface Science*, 636, 157779. <https://doi.org/10.1016/j.apsusc.2023.157779>

48. Haghightzadeh, A. (2020). Enhanced third-order optical susceptibility in Ag-doped CeO<sub>2</sub> nanostructures under pulsed Nd:YVO<sub>4</sub> laser. *Optics & Laser Technology*, 126, 106114. <https://doi.org/10.1016/j.optlastec.2020.106114>

49. Tiwari, M., Bhartiya, P. K., Bangruwa, N., Sarkar, S. K., & Mishra, D. (2024). Spin Polarization and Phase Transformation-Aided Efficient Overall Water Splitting Using Ni<sub>50</sub>Mn<sub>18</sub>Ga<sub>25</sub>Cu<sub>7</sub> Ferromagnetic Shape Memory Heusler Alloy. *ACS Applied Materials & Interfaces*, 16(50), 69398-69409. <https://doi.org/10.1021/acsami.4c15932>

50. Sagadevan, S., Johan, M. R., & Lett, J. A. (2019). Fabrication of reduced graphene oxide/CeO<sub>2</sub> nanocomposite for enhanced electrochemical performance. <https://doi.org/10.1007/s00339-019-2625-6>

51. Sagadevan, S., Johan, M. R., & Lett, J. A. (2019). Fabrication of reduced graphene oxide/CeO<sub>2</sub> nanocomposite for enhanced electrochemical performance. *Applied Physics A*, 125(5), 315. <https://doi.org/10.1007/s00339-019-2625-6>

52. Yousefali, S., Reyhani, A., Mortazavi, S. Z., Yousefali, N., & Rajabpour, A. (2018). UV-blue spectral downshifting of titanium dioxide nano-structures doped with nitrogen on the glass substrate to study its anti-bacterial properties on the E. coli bacteria. *Surfaces and interfaces*, 13, 11-21. <https://doi.org/10.1016/j.surfin.2018.07.003>

53. Dhanka, A. K., Kohlrausch, E. C., Samantray, R., Kumar, V., Pani, B., & Agasti, N. (2025). Harnessing defects in Ag/CeO<sub>2</sub> for enhanced photocatalytic degradation of antibiotic in water: Structural characteristics, in-depth insights on mechanism, degradation pathway. *Chemical Engineering Journal Advances*, 21, 100706. <https://doi.org/10.1016/j.ceja.2025.100706>

54. Selvaraj, S., Mohan, M. K., Navaneethan, M., Ponnusamy, S., & Muthamizhchelvan, C. (2019). Synthesis and photocatalytic activity of Gd doped ZnO nanoparticles for enhanced degradation of methylene blue under visible light. *Materials Science in Semiconductor Processing*, 103, 104622. <https://doi.org/10.1016/j.mssp.2019.104622>

55. Saranya, J., Ranjith, K. S., Saravanan, P., Mangalaraj, D., & Kumar, R. T. R. (2014). Cobalt-doped cerium oxide nanoparticles: enhanced photocatalytic activity under UV and visible light irradiation. *Materials science in semiconductor processing*, 26, 218-224. <https://doi.org/10.1016/j.mssp.2014.03.054>

56. Su, F., Li, P., Huang, J., Gu, M., Liu, Z., & Xu, Y. (2021). Photocatalytic degradation of organic dye and tetracycline by ternary Ag<sub>2</sub>O/AgBr–CeO<sub>2</sub> photocatalyst under visible-light irradiation. *Scientific Reports*, 11(1), 85. <https://doi.org/10.1038/s41598-020-76997-0>

57. Dhanka, A. K., Pani, B., & Agasti, N. (2025). Defect-enriched CuO/CeO<sub>2</sub> nanostructure: in-depth structural characterization and photocatalytic performance. *RSC advances*, 15(15), 11774-11789. <https://doi.org/10.1039/D5RA00640F>

58. Kazazi, M., Moradi, B., & Delshad Chermahini, M. (2019). Enhanced photocatalytic degradation of methyl orange using Ag/Sn-doped CeO<sub>2</sub> nanocomposite. *Journal of Materials Science: Materials in Electronics*, 30, 6116-6126. <https://doi.org/10.1007/s10854-019-00913-0>

59. Kumar, S., & Ojha, A. K. (2016). Ni, Co and Ni–Co codoping induced modification in shape, optical band gap and enhanced photocatalytic activity of CeO<sub>2</sub> nanostructures for photodegradation of methylene blue dye under visible light irradiation. *RSC advances*, 6(11), 8651-8660. <https://doi.org/10.1039/C5RA14184B>



60. Tamizhdurai, P., Sakthinathan, S., Chen, S. M., Shanthi, K., Sivasanker, S., & Sangeetha, P. (2017). Environmentally friendly synthesis of CeO<sub>2</sub> nanoparticles for the catalytic oxidation of benzyl alcohol to benzaldehyde and selective detection of nitrite. *Scientific reports*, 7(1), 46372. <https://doi.org/10.1038/srep46372>
61. Jayakumar, G., Irudayaraj, A. A., Raj, A. D., Sundaram, S. J., & Kaviyarasu, K. (2022). Electrical and magnetic properties of nanostructured Ni doped CeO<sub>2</sub> for optoelectronic applications. *Journal of Physics and Chemistry of Solids*, 160, 110369. <https://doi.org/10.1016/j.jpcs.2021.110369>
62. Muduli, S., & Sahoo, T. R. (2023). Green synthesis and characterization of CeO<sub>2</sub> and Ni-doped CeO<sub>2</sub> nanoparticles and its dielectric properties. *Materials Today: Proceedings*, 74, 697-702. <https://doi.org/10.1016/j.matpr.2022.10.278>
63. Mahmoudi Khatir, N., Abdul-Malek, Z., Zak, A. K., Akbari, A., & Sabbagh, F. (2016). Sol-gel grown Fe-doped ZnO nanoparticles: antibacterial and structural behaviors. *Journal of Sol-Gel Science and Technology*, 78(1), 91-98. <https://doi.org/10.1007/s10971-015-3922-y>
64. Mustapha, S., Ndamitso, M. M., Abdulkareem, A. S., Tijani, J. O., Shuaib, D. T., Mohammed, A. K., & Sumaila, A. (2019). Comparative study of crystallite size using Williamson-Hall and Debye-Scherrer plots for ZnO nanoparticles. *Advances in Natural Sciences: Nanoscience and Nanotechnology*, 10(4), 045013. <https://doi.org/10.1088/2043-6254/ab52f7>
65. Ren, Y., Jiang, Q., Yang, J., Luo, Y., Zhang, D., Cheng, Y., & Zhou, Z. (2016). Enhanced thermoelectric performance of MnTe via Cu doping with optimized carrier concentration. *Journal of Materiomics*, 2(2), 172-178. <https://doi.org/10.1016/j.jmat.2016.05.008>
66. Jafari, S., & Shaghaghi, Z. (2023). CeO<sub>2</sub>/CuO/NiO hybrid nanostructures loaded on N-doped reduced graphene oxide nanosheets as an efficient electrocatalyst for water oxidation and non-enzymatic glucose detection. *Dalton Transactions*, 52(22), 7564-7580. <https://doi.org/10.1039/D3DT00527E>
67. Zimou, J., Nouneh, K., Hsissou, R., El-Habib, A., El Gana, L., Talbi, A., & Addou, M. (2021). Structural, morphological, optical, and electrochemical properties of Co-doped CeO<sub>2</sub> thin films. *Materials Science in Semiconductor Processing*, 135, 106049. <https://doi.org/10.1016/j.mssp.2021.106049>
68. Kainbayev, N., Sriubas, M., Virbukas, D., Rutkuniene, Z., Bockute, K., Bolegenova, S., & Laukaitis, G. (2020). Raman study of nanocrystalline-doped ceria oxide thin films. *Coatings*, 10(5), 432. <https://doi.org/10.3390/coatings10050432>
69. Xu, Y., Miller, C. F., & Claiborne, L. L. (2024). Estimating Ce<sup>4+</sup> and Ce<sup>3+</sup> concentrations in zircon and coexisting melts, with implications for constraining oxygen fugacity. *Chemical Geology*, 663, 122283. <https://doi.org/10.1016/j.chemgeo.2024.122283>
70. Vigneshwaran, B., Kuppasami, P., Ajithkumar, S., & Kuppasamy, M. (2024). Temperature-dependent Raman and dielectric studies of Sm and Zr Co-doped BaTiO<sub>3</sub> ceramics. *Journal of Materials Science: Materials in Electronics*, 35(5), 353. <https://doi.org/10.1007/s10854-024-12060-2>
71. Negi, S. S., Kim, H. M., Cheon, B. S., Jeong, C. H., Roh, H. S., & Jeong, D. W. (2023). Restructuring Co-CoO<sub>x</sub> Interface with Titration Rate in Co/Nb-CeO<sub>2</sub> Catalysts for Higher Water-Gas Shift Performance. *ACS Applied Materials & Interfaces*, 15(44), 51013-51024. <https://doi.org/10.1021/acsami.3c09312>



72. Murugadoss, G., Kannappan, T., Rajabathar, J. R., Manavalan, R. K., Salammal, S. T., & Venkatesh, N. (2023). Rapid photocatalytic activity of crystalline CeO<sub>2</sub>-CuO-Cu(OH)<sub>2</sub> ternary nanocomposite. *Sustainability*, 15(21), 15601. <https://doi.org/10.3390/su152115601>
73. Tiwari, S., Rathore, G., Patra, N., Yadav, A. K., Bhattacharya, D., Jha, S. N., & Sen, S. (2019). Oxygen and cerium defects mediated changes in structural, optical and photoluminescence properties of Ni substituted CeO<sub>2</sub>. *Journal of Alloys and Compounds*, 782, 689-698. <https://doi.org/10.1016/j.jallcom.2018.12.009>
74. Wen, X. J., Niu, C. G., Zhang, L., Liang, C., & Zeng, G. M. (2018). A novel Ag<sub>2</sub>O/CeO<sub>2</sub> heterojunction photocatalysts for photocatalytic degradation of enrofloxacin: possible degradation pathways, mineralization activity and an in depth mechanism insight. *Applied Catalysis B: Environmental*, 221, 701-714. <https://doi.org/10.1016/j.apcatb.2017.09.060>
75. Zhang, K., Lv, S., Lin, Z., & Tang, D. (2017). CdS: Mn quantum dot-functionalized g-C<sub>3</sub>N<sub>4</sub> nanohybrids as signal-generation tags for photoelectrochemical immunoassay of prostate specific antigen coupling DNAzyme concatamer with enzymatic biocatalytic precipitation. *Biosensors and Bioelectronics*, 95, 34-40. <https://doi.org/10.1016/j.bios.2017.04.005>
76. Wang, M., Shen, M., Jin, X., Tian, J., Shao, Y., Zhang, L., & Shi, J. (2022). Exploring the enhancement effects of hetero-metal doping in CeO<sub>2</sub> on CO<sub>2</sub> photocatalytic reduction performance. *Chemical Engineering Journal*, 427, 130987. <https://doi.org/10.1016/j.cej.2021.130987>
77. Wang, L., Yu, Y., He, H., Zhang, Y., Qin, X., & Wang, B. (2017). Oxygen vacancy clusters essential for the catalytic activity of CeO<sub>2</sub> nanocubes for o-xylene oxidation. *Scientific reports*, 7(1), 1-11. <https://doi.org/10.1038/s41598-017-13178-6>
78. Murugan, R., Ravi, G., Vijayaprasath, G., Rajendran, S., Thaiyan, M., Nallappan, M., & Hayakawa, Y. (2017). Ni-CeO<sub>2</sub> spherical nanostructures for magnetic and electrochemical supercapacitor applications. *Physical Chemistry Chemical Physics*, 19(6), 4396-4404. <https://doi.org/10.1039/C6CP08281E>
79. Sideri, I. K., Arenal, R., & Tagmatarchis, N. (2025). Terpyridine-functionalized single-walled carbon nanotubes towards selectivity in the oxygen reduction reaction. *Nanoscale Advances*, 7(14), 4469-4479. <https://doi.org/10.1039/D5NA00281H>
80. Alla, S. K., Kollu, P., Meena, S. S., Poswal, H. K., Prajapat, C. L., Mandal, R. K., & Prasad, N. K. (2018). Investigation of magnetic properties for Hf<sup>4+</sup> substituted CeO<sub>2</sub> nanoparticles for spintronic applications. *Journal of Materials Science: Materials in Electronics*, 29(12), 10614-10623. <https://doi.org/10.1007/s10854-018-9125-x>
81. Zuo, S., He, Y., You, Y., Shu, X., Wen, M., Lu, Y., & Lu, X. (2023). Free occupying mechanism of simulated tetravalent waste ions in Gd<sub>2</sub>Zr<sub>2</sub>O<sub>7</sub> and performance evaluation of the waste forms. *Journal of the American Ceramic Society*, 106(11), 7088-7097. <https://doi.org/10.1111/jace.19303>
82. Bortamuly, R., Konwar, G., Boruah, P. K., Das, M. R., Mahanta, D., & Saikia, P. (2020). CeO<sub>2</sub>-PANI-HCl and CeO<sub>2</sub>-PANI-PTSA composites: synthesis, characterization, and utilization as supercapacitor electrode materials. *Ionics*, 26(11), 5747-5756. <https://doi.org/10.1007/s11581-020-03690-7>
83. Zheng, Y., Fu, K., Yu, Z., Su, Y., Han, R., & Liu, Q. (2022). Oxygen vacancies in a catalyst for VOCs oxidation:



synthesis, characterization, and catalytic effects. *Journal of Materials Chemistry A*, 10(27), 14171-14186. <https://doi.org/10.1039/D2TA03180A>

84. Yu, K., Lou, L. L., Liu, S., & Zhou, W. (2020). Asymmetric oxygen vacancies: the intrinsic redox active sites in metal oxide catalysts. *Advanced Science*, 7(2), 1901970. <https://doi.org/10.1002/advs.201901970>

85. Soni, S., Vats, V. S., Kumar, S., Dalela, B., Mishra, M., Meena, R. S., & Dalela, S. (2018). Structural, optical and magnetic properties of Fe-doped CeO<sub>2</sub> samples probed using X-ray photoelectron spectroscopy. *Journal of Materials Science: Materials in Electronics*, 29(12), 10141-10153. <https://doi.org/10.1007/s10854-018-9060-x>

86. Chen, J., Shen, S., Wu, P., & Guo, L. (2015). Nitrogen-doped CeO<sub>x</sub> nanoparticles modified graphitic carbon nitride for enhanced photocatalytic hydrogen production. *Green Chemistry*, 17(1), 509-517. <https://doi.org/10.1039/C4GC01683A>

87. Zou, X., Liu, J., Li, Y., Shen, Z., Zhu, X., Xia, Q., & Wang, Y. (2024). Molybdenum-doping promoted surface oxygen vacancy of CeO<sub>2</sub> for enhanced low-temperature CO<sub>2</sub> methanation over Ni-CeO<sub>2</sub> catalysts. *Applied Surface Science*, 661, 160087. <https://doi.org/10.1016/j.apsusc.2024.160087>

88. Mona, Y. (2024). Study on the electrochemical performance of Ni-doped ZnO nanorods utilized for the high-performance supercapacitor application. *Ionics*, 30(7), 4135-4142. <https://doi.org/10.1007/s11581-024-05588-0>

89. Hu, X., Tian, X., Lin, Y. W., & Wang, Z. (2019). Nickel foam and stainless steel mesh as electrocatalysts for hydrogen evolution reaction, oxygen evolution reaction and overall water splitting in alkaline media. *RSC advances*, 9(54), 31563-31571. <https://doi.org/10.1039/C9RA07258F>

90. Zou, X., Liu, J., Li, Y., Shen, Z., Zhu, X., Xia, Q., & Wang, Y. (2024). Molybdenum-doping promoted surface oxygen vacancy of CeO<sub>2</sub> for enhanced low-temperature CO<sub>2</sub> methanation over Ni-CeO<sub>2</sub> catalysts. *Applied Surface Science*, 661, 160087. <https://doi.org/10.1016/j.apsusc.2024.160087>

91. Sajith, N. V., Suresh, S., Bindu, M., Soumya, B. N., Kurup, M. P., & Periyat, P. (2022). Visible light active Ni<sup>2+</sup> doped CeO<sub>2</sub> nanoparticles for the removal of methylene blue dye from water. *Results in Engineering*, 16, 100664. <https://doi.org/10.1016/j.rineng.2022.100664>

92. Suen, N. T., Hung, S. F., Quan, Q., Zhang, N., Xu, Y. J., & Chen, H. M. (2017). Electrocatalysis for the oxygen evolution reaction: recent development and future perspectives. *Chemical Society Reviews*, 46(2), 337-365. <https://doi.org/10.1039/C6CS00328A>

93. Bao, F., Kemppainen, E., Dorbandt, I., Bors, R., Xi, F., Schlattmann, R., & Calnan, S. (2021). Understanding the hydrogen evolution reaction kinetics of electrodeposited nickel-molybdenum in acidic, near-neutral, and alkaline conditions. *ChemElectroChem*, 8(1), 195-208. <https://doi.org/10.1002/celec.202001436>

94. Tiwari, M., Bhartiya, P. K., Bangruwa, N., Sarkar, S. K., & Mishra, D. (2024). Spin polarization and phase transformation-aided efficient overall water splitting using Ni<sub>50</sub>Mn<sub>18</sub>Ga<sub>25</sub>Cu<sub>7</sub> ferromagnetic shape memory Heusler alloy. *ACS Applied Materials & Interfaces*, 16(50), 69398-69409. <https://pubs.acs.org/doi/full/10.1021/acsami.4c15932>

95. Zhiani, M., & Kamali, S. (2017). Synergistic effect of ceria on the structure and hydrogen evolution activity of nickel nanoparticles grown on reduced graphene oxide. *Journal of Materials Chemistry A*, 5(17), 8108-8116.



<https://doi.org/10.1039/C7TA00146K>

96. Tian, L., Liu, H., Zhang, B., Liu, Y., Lv, S., Pang, L., & Li, J. (2021). Ni and CeO<sub>2</sub> nanoparticles anchored on cicada-wing-like nitrogen-doped porous carbon as bifunctional catalysts for water splitting. *ACS Applied Nano Materials*, 5(1), 1252-1262. <https://doi.org/10.1021/acsnm.1c03850>
97. Gao, W., Xia, Z., Cao, F., Ho, J. C., Jiang, Z., & Qu, Y. (2018). Comprehensive understanding of the spatial configurations of CeO<sub>2</sub> in NiO for the electrocatalytic oxygen evolution reaction: embedded or surface-loaded. *Advanced Functional Materials*, 28(11), 1706056. <https://doi.org/10.1002/adfm.201706056>
98. Favaro, M., Drisdell, W. S., Marcus, M. A., Gregoire, J. M., Crumlin, E. J., Haber, J. A., & Yano, J. (2017). An operando investigation of (Ni–Fe–Co–Ce)O<sub>x</sub> system as highly efficient electrocatalyst for oxygen evolution reaction. *Acs Catalysis*, 7(2), 1248-1258. <https://doi.org/10.1021/acscatal.6b03126>
99. Chen, L., Jang, H., Kim, M. G., Qin, Q., Liu, X., & Cho, J. (2020). Fe x Ni y/CeO<sub>2</sub> loaded on N-doped nanocarbon as an advanced bifunctional electrocatalyst for the overall water splitting. *Inorganic Chemistry Frontiers*, 7(2), 470-476. <https://doi.org/10.1039/C9QI01251F>
100. Mishra, A. K., Willoughby, J., Estes, S. L., Kohler, K. C., & Brinkman, K. S. (2024). Impact of morphology and oxygen vacancy content in Ni, Fe co-doped ceria for efficient electrocatalyst based water splitting. *Nanoscale Advances*, 6(18), 4672-4682. <https://doi.org/10.1039/D4NA00500G>



## Data Availability

View Article Online  
DOI: 10.1039/D6MA00528D

The data supporting this article have been included as part of the Supplementary Information.

